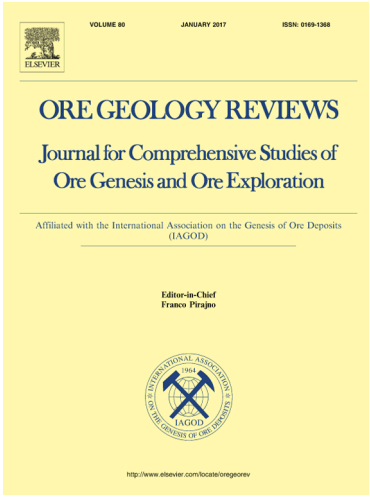

Actively forming Kuroko-type volcanic-hosted massive sulfide (VHMS) mineralization at Iheya North, Okinawa Trough, Japan

Christopher J. Yeats, Steven P. Hollis, Angela Halfpenny, Juan-Carlos Corona, Crystal LaFlamme, Gordon Southam, Marco Fiorentini, Richard J. Herrington, John Spratt

PII: S0169-1368(16)30140-8
DOI: http://dx.doi.org/10.1016/j.oregeorev.2016.12.014
Reference: OREGEO 2052

To appear in: *Ore Geology Reviews*

Received Date: 18 March 2016
Revised Date: 5 December 2016
Accepted Date: 8 December 2016

Please cite this article as: C.J. Yeats, S.P. Hollis, A. Halfpenny, J-C. Corona, C. LaFlamme, G. Southam, M. Fiorentini, R.J. Herrington, J. Spratt, Actively forming Kuroko-type volcanic-hosted massive sulfide (VHMS) mineralization at Iheya North, Okinawa Trough, Japan, *Ore Geology Reviews* (2016), doi: http://dx.doi.org/10.1016/j.oregeorev.2016.12.014

Actively forming Kuroko-type volcanic-hosted massive sulfide (VHMS) mineralization at Iheya North, Okinawa Trough, Japan

Christopher J. Yeats[1,2], Steven P. Hollis[1,3*], Angela Halfpenny[1,4], Juan-Carlos Corona[5], Crystal LaFlamme[6], Gordon Southam[7], Marco Fiorentini[6], Richard J. Herrington[8] & John Spratt[8]

[1]CSIRO, Mineral Resources, 26 Dick Perry Avenue, Kensington, Perth, Western Australia, 6151, Australia

[2]Geological Survey of New South Wales, NSW Department of Industry, 516 High St, Maitland, NSW, 2320, Australia

[3]iCRAG (Irish Centre for Research in Applied Geosciences) and School of Earth Sciences, University College Dublin, Belfield, Dublin 4, Ireland

[4]Microscopy & Microanalysis Facility, John de Laeter Center , Curtin University, Perth, Western Australia, 6102 , Australia

[5]Department of Geological Sciences and Environmental Studies, Binghamton University, Binghamton, NY, 13902, USA

[6]Centre for Exploration Targeting, School of Earth and Environment, University of Western Australia (M006), ARC Centre of Excellence for Core to Crust Fluid Systems, 35 Stirling Highway, Perth, Western Australia, 6009, Australia

[7]School of Earth Sciences, The University of Queensland, St Lucia, Queensland, 4072, Australia

[8]Department of Earth Sciences, Natural History Museum, London, SW7 5BD, UK

For: *Ore Geology Reviews (IF 3.558)*

Keywords: volcanogenic massive sulfide, VMS, hydrothermal, IODP, black smoker, EBSD

***Corresponding author:** steve.hollis@icrag-centre.org

ABSTRACT

Modern seafloor hydrothermal systems provide important insights into the formation and discovery of ancient volcanic-hosted massive sulfide (VHMS) deposits. In 2010, Integrated Ocean Drilling Program (IODP) Expedition 331 drilled five sites in the Iheya North hydrothermal field in the middle Okinawa Trough, back-arc basin, Japan. Hydrothermal alteration and sulfide mineralization is hosted in a geologically complex, mixed sequence of coarse, pumiceous, volcaniclastic and fine hemipelagic sediments, overlying a dacitic to rhyolitic volcanic substrate. At site C0016, located adjacent to the foot of the actively venting North Big Chimney massive sulfide mound, massive sphalerite-(pyrite-chalcopyrite±galena)-rich sulfides were intersected (to 30.2% Zn, 12.3% Pb, 2.68% Cu, 33.1 ppm Ag and 0.07 ppm Au) that strongly resemble the black ore of the Miocene-age Kuroko deposits of Japan. Sulfide mineralization shows clear evidence of formation through a combination of surface detrital and subsurface chemical processes, with at least some sphalerite precipitating into void space in the rock. Volcanic rocks beneath massive sulfides exhibit quartz-muscovite/illite and quartz-Mg-chlorite alteration reminiscent of VHMS proximal footwall alteration associated with Kuroko-type deposits, characterised by increasing MgO, Fe/Zn and Cu/Zn with depth. Recovered felsic footwall rocks are of FII to FIII affinity with well-developed negative Eu anomalies, consistent with VHMS-hosting felsic rocks in Phanerozoic ensialic arc/back-arc settings worldwide.

Site C0013, ~100 m east of North Big Chimney, represents a likely location of recent high temperature discharge, preserved as surficial coarse-grained sulfidic sediments (43.2% Zn, 4.4% Pb, 5.4% Cu, 42 ppm Ag and 0.02 ppm Au) containing high concentrations of As, Cd, Mo, Sb, and W. Near surface hydrothermal alteration is dominated by kaolinite and muscovite with locally abundant native sulfur, indicative of acidic hydrothermal fluids. Alteration grades to Mg-chlorite dominated assemblages at depths of >5 mbsf (metres below sea floor). Late coarse-grained anhydrite veining overprints earlier alteration and is interpreted to have precipitated from down welling seawater as hydrothermal activity waned. At site C0014, ~350 m farther east, hydrothermal assemblages are characterized by illite/montmorillonite, with Mg-chlorite present at depths below ~30 mbsf. Recovered lithologies from distal, recharge site C0017 are unaltered, with low MgO, Fe_2O_3 and base metal concentrations.

Mineralization and alteration assemblages are consistent with the Iheya North system representing a modern analogue for Kuroko-type VHMS mineralization. Fluid flow is focussed laterally along pumiceous volcaniclastic strata (compartmentalized between

impermeable hemipelagic sediments), and vertically along faults. The abundance of Fe-poor sphalerite and Mg-rich chlorite (clinochlore/penninite) is consistent with the lower Fe budget, temperature and higher oxidation state of felsic volcanic-hosted hydrothermal systems worldwide compared to Mid Ocean Ridge black smoker systems.

1. INTRODUCTION

Over the past 25 years our understanding of seafloor hydrothermal fields has been revolutionized by the research activity of the Deep Sea Drilling Project (1968-1983), Ocean Drilling Program (ODP; 1985-2003) and Integrated Ocean Drilling Program (IODP; 2004-2013). In particular, the research findings of expeditions to the Trans-Atlantic Geotraverse [TAG], Manus Basin and Juan de Fuca Ridge have provided important insights into the nature of fluid rock interaction and fluid mixing in the development of seafloor hydrothermal systems in different tectonic settings (Barriga et al., 2000; Fouquet et al., 1997; Humphris et al., 1995, 1998; Lackschewitz et al., 2004; Mottl et al., 1994; Paulick and Bach, 2006; Roberts et al., 2003; Teagle et al., 1998; Webber et al., 2011). This work has been complemented by countless other scientific and industry-funded cruises to hydrothermal fields worldwide (Connelly et al., 2012; de Ronde et al., 2005; Glasby et al., 2008; Hannington et al., 2005 and references therein; Ishibashi et al., 2015; McConachy et al., 2005; Petersen et al., 2014; Yeats et al., 2014; Webber et al., 2015).

Volcanic-hosted massive sulfide (VHMS) deposits represent significant resources of base and precious metals in a number of Archean Cratons and Phanerozoic volcanic arcs/back-arc basins worldwide (Barrie et al., 1993; Galley et al., 1993; Herrington et al., 2005; Hollis et al., 2015; van Staal, 2007). VHMS mineralization occurs as syngenetic stratiform accumulations of metal sulfides that precipitated at or below the seafloor, often underlain by discordant zones of stringer and disseminated sulfides (Franklin et al., 2005). The size, metallogeny and grade of a deposit that forms within a volcanic succession is dependent on its tectonic setting, host lithologies and any magmatic input (Barrie and Hannington, 1999; de Ronde et al., 2003, 2005; Piercey, 2011). Therefore, analogues for specific types of VHMS deposits are represented by different modern hydrothermal systems (e.g. Glasby et al., 2008; Hannington et al., 1998; Ishibashi and Urabe, 1995; Lüders et al., 2001; Webber et al., 2015). Active systems provide important insights into the formation of ancient VHMS deposits, allowing fluids to be directly sampled and mineralization to be studied without the effects of subsequent deformation and metamorphism.

Hydrothermal vents were first discovered at the Iheya North Knoll in 1995 (**Fig. 1**), and this location has since become the most intensely investigated of all hydrothermal fields within the middle Okinawa Trough, Japan (Aoyama et al., 2014; Chiba et al., 1996; Glasby and Notsu, 2003; Ishibashi et al., 2015; Kawagucci et al., 2013; Masaki et al., 2011; Shao et al., 2015; Takai et al., 2011; Tsuji et al., 2012). During 2010, IODP Expedition 331 drilled five sites at Iheya North. Blocks of massive and semi-massive sphalerite-(pyrite-chalcopyrite±galena)-rich sulfides, that strongly resembled the 'black ore' of the Kuroko VHMS deposits of Japan, were recovered from immediately beneath the modern seafloor (Takai et al., 2011). Samples collected during IODP Expedition 331 provide a unique opportunity to understand hydrothermal fluid flow and mineralization processes associated with an actively forming Kuroko-style VHMS deposit in an ensialic back-arc setting. We present shipboard logging and X-ray diffraction data, along with new petrographic, whole rock geochemical, mineral- chemical and microstructural work on recovered lithologies.

2. REGIONAL GEOLOGY

The Okinawa Trough, Japan, extends for ~1200 km between the Ryukyu arc-trench system and the Eurasian continent, and is regarded as an incipient intra-continental back-arc basin (Lee et al., 1980; Letouzey and Kimura, 1986; Shinjo and Kato, 2000; **Fig. 1a**). It is still considered to be in an early rifting stage prior to seafloor spreading (Shinjo and Kato, 2000), with a minimal crustal thickness of ~8 km at its southernmost end (Klingelhoefer et al., 2009). Arc volcanism predominantly occurs in the northern part of the Ryukyu Arc and in the middle and southern parts of the Okinawa Trough (Shinjo et al., 2000). The transition from arc to back-arc volcanism in the middle Okinawa Trough has been termed the VAMP area (Sibuet et al., 1987), with present day activity in the middle and southern Okinawa Trough associated with *en echelon* intra-trough grabens (Glasby and Notsu, 2003; Shinjo and Kato, 2000). The VAMP area is coincident with the subduction of the WNW-ENE trending Daito Ridge (Sibuet et al., 1998; **Fig. 1a**). A rift-related bimodal basaltic-rhyolitic suite, accompanied by minor intermediate rocks, characterizes the middle Okinawa Trough (Ishizuka et al., 1990; Shinjo et al., 1999; Shinjo and Kato, 2000; Zeng et al., 2010). Thick (~1000 m) sequences of organic-rich terrigenous sediments sourced from the Yangtze and Yellow rivers overlie basement lithologies (Takai et al., 2011). Due to volcanism and rifting, the VAMP area is characterized by anomalously high heat flow (Yamano et al., 1986) and contains several hydrothermal fields (Glasby and Notsu, 2003; Ishibashi et al., 2015). From

north to south these include the Minami-Ensei Knoll, Iheya North Knoll (**Fig. 1b-c**), Yoron Hole, CLAM site of the Iheya Ridge, the JADE and Hakueri hydrothermal fields of the Izena Hole (also known as the Izena Cauldron) (Ishibashi et al., 2015).

3. HYDROTHERMAL ACTIVITY AT IHEYA NORTH

The Iheya North Knoll hydrothermal field is located at ~1000 mbsl (metres below sea level) in the middle Okinawa Trough (**Fig. 1b**). Approximately ten hydrothermal mounds aligned north to south are associated with active venting and sulfide/sulfate mineralization (Ishibashi et al., 2015; **Fig. 1c**). The main sulfide assemblages identified from chimney samples are dominated by sphalerite, wurtzite [(Zn,Fe)S], galena, pyrite, marcasite [FeS_2] and chalcopyrite (Ueno et al., 2003). Some samples also include arsenopyrite, tetrahedrite [$Cu_{12}(As,Sb)_4S_{13}$], tennantite [$Cu_3(As,Sb)_4$], freslebenite [$PbAgSbS_3$], native arsenic, realgar [AsS] and/or covellite [CuS] (Ueno et al., 2003). Gangue mineralogy is characterized by barite, gypsum, anhydrite, quartz, rhodochrosite [$MnCO_3$], and/or native sulfur (Chiba, 1997; Ueno et al., 2003).

Recent studies of hydrothermal fluid chemistry at Iheya North indicate the presence of high concentrations of CO_2, CH_4, NH_4^+, B, and I, and high alkalinity, consistent with some interaction between hydrothermal fluids and organic matter (Kawagucci et al., 2011), although this is less pronounced than at the JADE and CLAM sites. High concentrations of K, Rb, Cs and Li in interstitial water are consistent with interaction between hydrothermal fluids and felsic footwall lithologies (Takai et al., 2011). North Big Chimney (NBC) marks the centre of the hydrothermal field and is associated with the vigorous venting of clear fluid of 311 °C at 971 mbsl (Nakagawa et al., 2005; **Fig. 1c**). The chimney is 20 m high and 6 m in diameter (Takai et al., 2011). Chloride concentrations lower than seawater suggest phase separation at depth (Chiba et al., 1996).

During IODP Expedition 331, five sites were drilled at Iheya North (C0013 to C0017; **Figs. 1b-c, 2**). Hydrothermal alteration and sulfide mineralization is hosted in a geologically complex mixed sequence of coarse pumiceous, volcaniclastic, and fine, hemipelagic, sediments, overlying dacitic to rhyolitic volcanic substrate. Site descriptions (section 5) are based on shipboard data (detailed in Takai et al., 2011, 2012) and post-cruise research. Post-drilling changes in fluid flow and chemistry at sites C0014 and C0016 are detailed in Kawagucci et al. (2013).

4. METHODS

During IODP Expedition 331, approximately 325 powdered whole rock samples were analysed by X-ray diffraction (XRD) to characterize the main alteration minerals present across the Iheya North hydrothermal field. Samples of interest were also examined using polished thin sections and scanning-electron microscopy (SEM). Post-cruise research focussed primarily on the whole rock geochemical, mineral-chemical and microstructural characterization of recovered lithologies.

Shipboard SEM analysis was conducted using a GEOL 5770 SEM equipped with backscatter and energy dispersive spectroscopy detectors operating at an accelerating voltage of 15 kV. Samples for XRD were systematically analysed from every 1.5 m section of core obtained during hydraulic piston coring and extended shoe coring, and for every 0.75 m core section for Baker Hughes INTEQ (BHI) cores. Additional samples were analysed as deemed appropriate. Samples were freeze-dried prior to powdering in a ball mill. Powders were analysed on a PANalytical CubiX PRO (PW3800) diffractometer. Further detail is provided by Takai et al. (2011).

For post-cruise research, samples from site C0016 were imaged using both secondary electrons (SE) and backscattered electrons (BSE) in a Zeiss Ultraplus field emission gun (FEG) SEM at the CSIRO facilities, Kensington, Western Australia, operated at a chamber pressure of $2x10^{-6}$ mbar and an accelerating voltage of 20 kV.

Twenty-five specimens (samples IN01-IN25) representative from each of the five sites (C0013 to C0017) were submitted for whole-rock geochemical analysis to Bureau Veritas Geoanalytical Laboratory, Canning Vale, Western Australia, to characterize the geochemistry of the host sequence and the intensity of hydrothermal alteration. Samples were predominantly composed of variably hydrothermally altered and/or mineralized, felsic pumiceous volcaniclastic sediments and basement rocks, with one sample of hemipelagic clay (IN08; **Table 1**). Major element concentrations (plus S, Cu, Pb, Zn, Ba) were determined on fused glass beads (using a 12:22 flux ratio and 4% lithium nitrate) by X-ray Fluorescence (XRF). Trace elements were determined on the same fused discs by laser ablation inductively coupled plasma mass spectrometry (LA-ICP-MS). Gold, Pt and Pd were analysed by lead-collection fire assay with element concentrations quantified by ICP-MS. Carbon concentrations were measured by total combustion using a Carbon-Sulfur Analyser. Loss on ignition (LOI) was calculated using a robotic thermogravimetric system set to 110 and 1000 °C. Sulfate concentrations were determined by digestion with hydrochloric acid and evaporation to dryness twice before a final leach in hydrochloric acid. Results are presented in **Table 1**.

Accuracy (% RD) was monitored using mineralized (to 34.6% Zn, 13.2% Pb, 3.1% Cu) and unmineralized international standards. Precision (% RSD) was monitored by repeat analysis of samples from Iheya North. Accuracy and precision can be considered good to excellent after Jenner (1996) for all elements determined by XRF, except for Al_2O_3, MgO, MnO and P_2O_5 in some instances where concentrations were near detection (i.e. 0.01 wt.%). Accuracy for elements determined by LA-ICP-MS was good to excellent (<10% RD) except for As at low concentrations, and Cd. Precision was also poor (>10% RSD) for Cd and consequently these data should be treated with caution. Accuracy and precision for Au, Pt, Pd and C were good to excellent for all standards used after Jenner (1996).

Mineral compositions of chlorite and white mica from site C0016B were determined at the Natural History Museum, London, on a Cameca SX-50 Electron Microprobe (EMP) equipped with a wavelength dispersive system (WDS). Operating conditions were at 20 keV and 20 nA. Counting times ranged from 10 to 50 s for spot analysis. Chlorite mineral formulae were calculated using the worksheets of Tindle (2015).

For EBSD analysis, round samples (25 mm in diameter) were polished using colloidal silica for 5 hours on a Buehler Vibromat 1, and for 1 hour on the Leica Microsystems EM RES101 instrument (after Halfpenny, 2010; Halfpenny et al., 2013). Full crystallographic orientation data were obtained from automatically indexed Kikuchi diffraction patterns collected using a Bruker e-flash detector fitted to a Zeiss Ultraplus FEG SEM at the CSIRO facilities, Kensington. Coincident EDS data were collected using a Bruker XFlash 5030 detector. The SEM was operated using an accelerating voltage of 20 kV and a 120 µm aperture, which in high current mode produced a beam current of 12.1 nA. The EBSD data were collected using the Bruker Quantax Espirit 1.9 software, using a resolution of 200 x 150 pixels, a 12 ms exposure time and a step size between measurements of 1.7 µm. If the pattern quality was poor then the software was unable to find the correct crystallographic solution and the point was not indexed. Non-indexed points are common in areas of poor surface quality, on grain boundaries, cracks, void space and where the surface is contaminated. Unfortunately, not all of the sample was prepared well enough for EBSD analysis, due to the various hardnesses of the constituent phases, this has led to areas of non-indexing. The EBSD data were post-processed using Oxford Instruments Channel 5 software to remove mis-indexed points and interpolate non-indexed points (Prior et al., 2009; Halfpenny, 2010). The corrected data files were then used to generate the maps presented.

5. RESULTS

5.1 Hydrothermal alteration and mineralization at Iheya North

Site C0016 (North Big Chimney)

Site C0016 is located at North Big Chimney (**Fig. 1c**). Although hole C0016A at the summit of NBC failed to recover core, a variety of lithologies were obtained from hole C0016B drilled at its base (**Fig. 3f-j**). From 45 m of drilling at C0016B, only 2.1 m of core was recovered (4.7% recovery). Between 0 and 9 mbsf, blocks of massive and semi-massive sphalerite-rich sulfide were recovered (**Fig. 3f** –1 to 3), along with a 15cm section of silicified and mineralized volcanic rock altered to illite/muscovite clay (confirmed by XRD; **Fig. 3g**). Recovered sections of clastic-textured massive/semi-massive sulfide (**Fig. 3f** – blocks 1 to 3) are characterized by rounded 1-5 mm fragments of clay-altered and hard siliceous volcanic rock, cemented by a matrix of sphalerite (~60%), pyrite (~15%) and quartz, with lesser galena and chalcopyrite (**Figs. 3f; 4a**). Silicification is variable, with the uppermost block containing coarser grained (2-3 mm) sphalerite-pyrite-galena-(chalcopyrite) associated with late anhydrite veining (**Fig. 3f**). The second section of core obtained from 9-27 mbsf (31 cm total recovery) included two pieces of hydrothermally altered, silicified and mineralized volcanic rock with clastic textures, found either side of a 12 cm piece of coarsely crystalline white acicular anhydrite cut by thin veins of sphalerite-pyrite (**Fig. 3h** - blocks 5-7). The third section of core (from 27-45 mbsf) comprised almost 1m of quartz-chlorite altered volcanic rock exhibiting stockwork veining of quartz-chlorite-pyrite and late anhydrite (**Fig. 3i-j –** blocks 8-9). XRD analysis identified the chlorite as clinochlore (Mg-chlorite) – subsequently confirmed by electron microprobe analysis. Two generations of veining have been recognized: (i) early sugary, 2-3 cm wide quartz-chlorite-pyrite veins which form a dark network; and (ii) late vuggy pyrite-anhydrite veins, from hairline to 1 cm in thickness.

Site C0013 (a site of recent hydrothermal activity):

Site C0013, located ~100 m east of NBC (Fig. 1c), is characterized by numerous areas of patchy diffuse flow and chemosynthetic animal colonies, where the seafloor is covered by pumiceous breccias and barite-anhydrite-carbonate crusts, with hemipelagic sediment in depressions (Takai et al., 2012). Site C0013 occurs in a zone of relatively high heat flow, estimated before drilling to be ~3 °C/m (Takai et al., 2012). Eight holes were sited to a maximum depth of 54.3 mbsf (hole C0013E; Fig. 2a). Melting of plastic core liners severely limited drilling to depth, with core liners starting to soften and deform at 12 mbsf and 82 °C. Following capping and casing of the deepest hole, strong hydrothermal discharge was noted

by ROV from the casing pipe, with thermoseal temperature-sensitive strips indicating temperatures >250 °C. Two days later blackish water was discharging directly from the hole beneath the guide base.

Eight holes were drilled at site C0013 (A to H). Due to their close proximity, core from these holes exhibit a broadly consistent vertical distribution (**Fig. 2a**). From 0 to ~4 mbsf moderately hydrothermally altered sulfidic sediment was recovered from several holes, characterized by detrital sulfide (sphalerite-pyrite-covellite), sulfate (anhydrite-barite), kaolinite-muscovite (confirmed by XRD) and locally, native sulfur. Native sulfur occurs as veinlets, cements (**Fig. 3c**), and coatings in voids (**Fig. 3d**). Rapid lateral and vertical variations in the composition and grain size of the sulfidic sediments suggest they originated locally, probably from the breakdown of nearby hydrothermal mounds and/or chimney structures. Thin horizons (~10 cm) can exceed 50% sulfide (e.g. C0013E). Covellite is much less abundant than sphalerite and pyrite (**Fig. 4e-f**), and framboidal pyrite was also observed (**Fig. 4g-h**). The sediment is commonly poorly sorted, medium- to coarse-grained, and contains anhydrite crystal fragments and lesser barite. Anhydrite shows evidence for incipient dissolution and replacement by gypsum (**Fig. 4i**). SEM analysis also identified galena and tetrahedrite-tennantite intergrowths with sphalerite, and an unknown silver arsenide phase associated with opaline silica (**Fig. 4j**). Underlying pale grey to white sediments (from ~4 to ~5.5 mbsf) are characterized by an assemblage of kaolinite-muscovite-anhydrite, with trace fine-grained disseminated pyrite.

From ~5.5 to ~26 mbsf, site C0013 is dominated by pale bluish-grey to white mottled hydrothermal clay. Mg-chlorite (clinochlore) was identified as the main alteration mineral by XRD, and occurs with coarse (4-5 cm) rounded nodules of brecciated, drilling-disturbed veins of white, opaque, anhydrite ± dolomite ± talc ± calcite ± quartz ± sphalerite ± pyrite (**Fig. 3a**), which show evidence for erosion. Fine-grained disseminated pyrite and sphalerite are present in low abundances (<1%), and rare irregular veins of anhydrite-sulfide and quartz-sulfide cut the Mg-chlorite altered sediments.

Quartz and Mg-chlorite altered volcanic basement was recovered from below ~26 mbsf in holes C0013D and C0013E (**Fig. 3b**). The rocks are unique in their hardness and distinct quartz stockwork veining (most of which are barren of sulfides). Petrographic analysis has revealed that ~40% of the rock is composed of volcanic glass, with the remainder devitrified and replaced by quartz-chlorite and minor biotite. Rare mineralized quartz veins contain sphalerite, pyrite, covellite, and in one interval, fine intergrowths of

native copper and organic carbon (**Fig. 3e**). Overlapping the zones of kaolinite and Mg-chlorite alteration, abundant 1-2 cm euhedral anhydrite crystals occur in the core (**Fig. 2a**).

Site C0014 (distal alteration and mineralization):

Site C0014 is located 350 m east of site C0013 (**Fig. 1c**) and ~450 m from the NBC hydrothermal mound. A distinct colony of clams and a rocky seafloor characterize the site (Takai et al., 2012). Seven holes were drilled to a maximum depth of 136.7 mbsf (hole C0014G; **Fig. 2b**). Compared to the two sites described above, site C0014 is dominated by lower temperature alteration assemblages and is only weakly mineralized (**Fig. 2b**). From 0 to 8-10 mbsf, hemipelagic ooze and pumiceous volcaniclastic sediments exhibit little evidence of hydrothermal alteration (except weak oxidation in holes C0014F and C0014G), with quartz, muscovite and calcite the most abundant phases determined by XRD. Sulfides commonly occur as fine-grained disseminated and framboidal pyrite grains. An underlying zone of pale grey mottled clay is characterized dominated by quartz-muscovite and alteration minerals illite-montmorillonite with lesser kaolinite.

Below ~25-30 mbsf (to the maximum depth of 136.7m; hole C0014G) Mg-chlorite becomes an important alteration phase irrespective of lithology (**Fig. 2b**). Unlike at site C0013, detrital muscovite and quartz persist. Anhydrite is present, but is significantly less abundant with only mm-scale irregular veinlets, with halite below 57 mbsf. After casing and capping, diffuse hydrothermal fluids were observed by ROV, discharging from the seafloor through the space between the wall of the hole and the casing pipe (Takai et al., 2012). Thermoseal strips indicated the diffusing fluids were >240 °C (Takai et al., 2012).

In the illite-montmorillonite and Mg-chlorite zones little sulfide mineralization was observed. Pyrite occurs in trace amounts disseminated throughout the core (**Fig. 4k**) and very rarely as coarser veins (with sphalerite-galena-chalcopyrite; **Fig. 4l**). XRD analysis also identified covellite in some sections of core, although none was identified under binocular microscope.

Site C0015

Site C0015 is located ~600 m northwest of NBC (**Fig. 1b**). Hole C0015C was the deepest at the site, drilled to only 9.4 mbsf. No hydrothermal alteration was observed. Evidence for weak oxidation in the uppermost layers included orange to brown iron oxide staining on pumice fragments. The area is characterized by a low surface temperature gradient of 1 °C/m (Takai et al., 2012). Together with the presence of iron oxides and

characteristic major element compositions of interstitial water samples close to those of seawater, the relatively low temperature gradient suggests that the site represents a background site, unrelated to the hydrothermal system (Takai et al., 2012).

Site C0017 (a distal recharge site)

Site C0017 is located ~1.6 km east of North Big Chimney (**Fig. 1b**) and is characterized by extremely low heat flow, with a surface thermal gradient an order of magnitude lower than the average non-hydrothermal, trough-filling sediments of the middle Okinawa Trough (Takai et al., 2012). Hole C0017D was the deepest (150.6 mbsf) across all sites during IODP Expedition 331, recording a temperature of only 90 ± 5 °C at the base of the hole. Sediment types encountered were homogeneous hemipelagic mud, pumiceous sediment, and volcaniclastic-pumiceous breccia and mixed sand with erosional bases. No alteration was observed except weak to moderate oxidation, which was reflected in a yellow to brownish colouration in sediments, orange to brown iron oxide staining on pumice fragments, and 1-2 mm botryoidal aggregates of Fe-Si oxyhydroxides. Geochemical results, including reversals in alkalinity, ammonium and phosphate pore water concentrations, combined with downhole temperature measurements, indicate that this oxidized zone resulted from cold seawater influx (Takai et al., 2011, 2012). Notably, sulfides were absent at shallow depths, with trace pyrite consistently present below 94 mbsf.

5.2 Texture analysis

EBSD analysis was performed as it reveals information on crystal orientation, grain boundaries and phase distribution (Prior et al., 1999). EBSD data may be used to understand the controlling mineralization processes and determine any subsequent modification. Three samples were analysed, all from site C0016 - two samples of sphalerite-rich semi-massive sulfides (16B-2, 16B-3; **Fig. 3f**- blocks 2 and 3 respectively) and a quartz-chlorite altered volcanic rock with stringer and disseminated sulfides (16B-9; **Fig. 3** – block 9). For both samples of semi-massive sulfide, two areas were analysed (denoted by A and B).

For EBSD analysis, the interface between two grains is termed the grain boundary. Where the minimum misorientation angle is >10° these are termed high angle grain boundaries (HAGBs) (Halfpenny et al., 2012). Low angle grain boundaries (LAGBs) or sub-grain boundaries have misorientation angles of <10° and are composed of an array of dislocations (Halfpenny et al., 2006; Trimby et al., 1998). LAGBs represent intra-grain variations due to modification of the grains post-mineralization. There are some special

orientations where there is a relationship between the lattices on either side of a boundary. One such structure is a coincident site lattice (CSL), which describes the number of atoms that are shared on the boundary between the grains. For coherent twin boundaries Σ3, one in three atoms is shared. If the crystallographic orientations of an individual phase are fully random, then there is no distinct texture. However, in some geological systems grains can align due to mineralization and deformation processes producing a crystallographic preferred orientation (CPO) (Halfpenny, 2011; Halfpenny and Prior, 2009). If a CPO is identified it may be used to interpret the underlying processes which caused grain alignment (Fougerouse et al., 2016a; Fougerouse et al., 2016b).

Sample 16B-2 is dominated by sphalerite, with lesser pyrite, chalcopyrite, quartz, chlorite and graphite. Two areas within this sample were analysed - 16B-2A (**Fig. 5a-c**) and 16B-2B (**Fig. 5d-f**). In the prior, sphalerite exhibits a variable grain size with the grain diameter varying from 10-20µm. The sphalerite exhibits Σ3 (60°±5° about <111>) CSLs (red lines) and very little substructure development as there are few LAGBs (white lines) (**Fig. 5c**). None of the indexed phases in area 16B-2A exhibit a CPO. In area 16B-2B, the sphalerite exhibits a coarser grain size with a maximum of grain diameter of 47 µm. Sphalerite grains contain multiple Σ3 CSL's (**Fig. 5f**). All phases measured show little to no internal deformation (no LAGBs) and no CPO has been developed.

Sample 16B-3 contains sphalerite as the main phase with quartz, chlorite, pyrite, chalcopyrite, anhydrite and minor amounts of graphite (**Fig. 5g-l**). In area 16B-3A, the sphalerite is coarse grained, contains Σ3 CSLs and some of the sphalerite grains exhibit lobate grain boundaries (**Fig. 5i**). In area 16B-3B, the sphalerite is extremely coarse grained and exhibits lobate grain boundaries (**Fig. 5j & k**). There is a small area which contains finer grained sphalerite and pyrite crystals (**Fig. 5l**). None of the indexed phases in sample 16B-3 exhibit a CPO or internal deformation (**Fig. 5l**).

Sample 16B-9 is from a pyrite vein and the mineralogy is dominantly pyrite and quartz with some chlorite (**Fig. 5m & n**). The pyrite exhibits a bimodal grain size distribution between coarse (>40 µm in diameter) and fine grains (<40 µm in diameter). The quartz crystals range from euhedral to anhedral, but all grains exhibit little to no internal deformation (**Fig. 5o**). No CPO is observed.

5.3. Whole rock geochemistry

Massive sulfide from site C0016B (sample IN01) contains high concentrations of Zn (30.2%), Pb (12.3%) and Cu (2.68%), and elevated Mo (35.4 ppm), Ag (33.1 ppm), Sb (25.6

ppm) and Au (0.07 ppm) with respect to unmineralized samples from Iheya North. Low concentrations of lithophile elements, such as SiO_2 (4.9 wt.%), Al_2O_3 (0.21 wt.%), MgO (0.28 wt.%) and K_2O (0.11 wt.%), are consistent with large mass gains of Fe, S and base metals (see following section). Underlying felsic rocks (**Fig. 6a**) from site C0016 contain significantly lower levels of Fe, Zn, Cu, Pb, Sb, Mo, Ag and Au (**Table 1**). Increasing MgO, Cu/Zn and Fe/Zn occur down hole in C0016B. MgO values are low (0.3 wt.%) in massive sulfides (IN01), ~1.0 wt.% in underlying silicified volcanic rocks (IN02-IN04), and 5.2-5.8 wt.% in quartz-chlorite altered rocks at depth (IN05-IN06). Quartz-chlorite altered rocks are also characterized by much higher Fe/Zn (917-1044) and Cu/Zn ratios (0.5-0.6) than overlying lithologies (<6.0 Fe/Zn and <0.1 Cu/Zn). SiO_2, K_2O, sulfide and sulfate concentrations are erratic down hole C0016B due to varying degrees of silicification, sulfide mineralization and anhydrite veining. Na_2O concentrations are consistently ~0.1 wt.% throughout, indicative of extensive feldspar destruction or an absence of albite in the rhyolitic precursor. On the Box Plot of Large et al. (2001a; see figure caption for description), samples from C0016B plot on a chlorite-pyrite-(sericite) trend, away from the least altered dacite field, characterized by high CCPI (Carbonate-chlorite-pyrite Index) and Alteration Index values (**Fig. 6b**).

Samples from site C0013 are in many respects geochemically similar to those from site C0016 (**Table 1**). A sample of coarse grained sulfidic sediment from C0013 (IN13) is characterized by high Zn (43.2%), Fe_2O_3 (9.6%), Cu (5.4%), Pb (4.4%), As (1.5%), Ag (42 ppm), Cd (980 ppm) Sb (104 ppm) and Mo (59 ppm). This is consistent with the presence of abundant coarse sphalerite (overgrown by pyrite), covellite (**Fig. 4e**) and chalcopyrite identified under binocular microscope in near surface sulfidic sediments. Galena and sulfosalts, including tetrahedrite-tennantite, were identified by SEM and are intergrown with sphalerite. High concentrations of Zn (3.46%) and Cu (1.89%) also occur in samples with visible sulfide veining at depth (e.g. sample IN16). SiO_2, K_2O, MgO, Fe_2O_3, Na_2O, S and base metal concentrations are erratic throughout the sampled sections. Samples from C0013 with significant anhydrite are characterized by high CCPI and low Alteration Index values near the calcite mineral node of the Box Plot (**Fig. 6b**).

Zinc concentrations from the relatively distal site C0014 (to 0.01% Zn) are consistently lower than at sites C0013 and C0016. Hydrothermal alteration at C0014 is dominated by quartz and muscovite with minor kaolinite, illite/montmorillonite, and Mg-chlorite at depth. This is reflected by varying concentrations of SiO_2, K_2O, Na_2O, CaO, MgO and Al_2O_3. Na_2O concentrations are significantly higher (0.3-0.92 wt.%) than at proximal

sites C0013 and C0016. Iron and base metal concentrations are low in all samples (<4.47 wt.% Fe_2O_3 and <0.02% Cu+Pb+Zn) due to the lack of sulfides. Discounting rare anhydrite-rich units, samples from C0014 are characterized by high Alteration Index and moderate CCPI values, typical of a distal sericite-chlorite-pyrite trend (Large et al., 2001a; **Fig. 6b**). At site C0014, Sb concentrations reach a maximum of ~7.1 ppm, which are significantly lower than at proximal sites C0016 and C0013.

Samples of felsic pumice and clay from sites C0015 and C0017 are characterized by low MgO (0.37-0.62 wt.%), Fe_2O_3 (2.3-5.3 wt.%), LOI (<6 wt.%) and base metal concentrations (<0.04% Cu+Pb+Zn). SiO_2 concentrations for pumice samples (67.8-69.4 wt.%) are typical of unaltered felsic rocks. All three samples analysed plot within the least altered dacite and rhyolite fields on the Box Plot of Large et al. (2001a) (**Fig. 6b**), containing low concentrations of Au, Ag, Bi, Cu, Mo, Pb, Sb, Te, Tl and Zn (**Table 1**).

Immobile element geochemistry: Most lithologies sampled from Iheya North are of felsic composition (**Fig. 6a**), characterized by high Zr/TiO_2 ratios. Three clay-rich samples plot closer to the intermediate field of Pearce (1996), along with massive sulfides from C0016B. These include one sample of hemipelagic clay (IN08), and two samples dominated by illite/montmorillonite (IN19, IN20). Felsic lithologies (both pumiceous volcaniclastic sediments and coherent volcanic basement) are of FII to FIIIa affinity according to the VHMS fertility diagrams of Lesher et al. (1986) and Hart et al. (2004) (**Fig. 6c**); and straddle the volcanic arc and A-type fields of Pearce et al. (1984; **Fig. 6d**). This latter diagram is shown simply to highlight the HFSE enrichment of the felsic rocks (after Piercey, 2011). With increasing mass gain at sites C0016, C0013 and C0014, Nb and Y concentrations will be diluted at a constant ratio as both elements are immobile (see arrow in **Fig. 6d**). All samples analysed herein display prominent negative Eu anomalies on chondrite-normalized REE diagrams, with slightly elevated LREE concentrations and flattish HREE profiles (**Fig. 6e**). Elevated HFSE concentrations (e.g. **Fig. 6d**), and Sc/V and Sc/TiO_2 ratios, are consistent with felsic rocks associated with VHMS deposits in ensialic settings worldwide (see Piercey, 2011; Hollis et al. 2015 and references therein).

Mass change: Mass change values were calculated for selected samples from across the Iheya North hydrothermal field using the isocon method of Grant (1986, 2004). Isocons were fitted using a range of immobile elements: Al, Ga, Hf, La, Nb, P, Ta, Tb, Ti, Th, Y, Yb, Zr (**Figure 7**). Element concentrations are scaled for plotting convenience using the values listed

in **Table 2**. Sample IN07 (grey woody pumice) from site C0017 was used for a least altered composition, consistent with shipboard XRD and petrographic analysis. Although this pumice may have been introduced from elsewhere, its similar Zr/TiO_2, Nb/Y, La/Yb_{CN} and Zr/Y ratios (**Fig. 6**) suggest it is of similar composition to the altered felsic volcanic/volcaniclastic rocks of sites C0016, C0013 and C0014. Calculated mass change values are illustrated in **Figure 8** and provided in **Table 3**. Mineralized and hydrothermally altered samples from sites C0016, C0014 and C0013 show significant mass gains in Cu-Pb-Zn-Fe-S-Au-Ag-As-Sb-Bi-Mo-Sr-Sn-Te-Tl-Mg-LOI±Si±Ca and losses of Na-K-Cs-Eu-Rb±Ba (**Fig. 8**). Mass change is most pronounced in the massive sulfides from site C0016, with large gains of Fe, S, Cu, Pb, Zn and a range of trace metals (e.g. Ag, As, Mo, Sb, Te) as to be expected, decreasing downhole (samples IN01, IN02 and IN05: **Fig. 8**). Less well mineralized footwall rocks show smaller gains of Fe, S, base and trace metals. Erratic gains of Si and Mg are due to variable silicification and chloritization. Samples from more distal sites C0013 and C0015 (represented by IN15 and IN09 respectively) have lower mass gains and losses than samples from site C0016. The clustering of mobile elements around the isocon of sample IN09 (**Fig. 7**) is consistent with the unaltered nature of site C0015, with only minor losses of SiO_2, and gains of Sr and Ba (**Fig. 8**).

5.4 Mineral chemistry

Three samples from site C0016 were characterized by electron microprobe analysis: 16B-1 (sphalerite-rich massive sulfide, from 0-9 mbsf; **Figure 3f-1**), 16B1-3 (silicified and anhydrite-sulfide veined volcanic rock, from 0-9 mbsf; **Fig. 3g**), and 16B-8 (quartz-chlorite altered volcanic rock from 27-45 mbsf; **Fig. 3i**). Chlorite analyses (n=42) plot consistently within the clinochlore and penninite fields (**Fig. 9**), characterized by extremely low Fe/Fe+Mg and moderate Si. Chlorite geothermometers (MacLean and Kranidotis, 1987; Zhang and Fyfe, 1995) yield average temperature estimates of 218-235 °C for sphalerite-rich massive sulfides (sample 16B-1), and 225-241 °C for quartz-chlorite altered volcanic rock (sample 16B-8).

White mica was analysed from sample 16B1-3 (a silicified and anhydrite-sulfide veined volcanic rock from 0-9mbsf) and was not identified in the other two samples discussed above. Mg/(Fe+Mg) ratios are high 0.90-0.94 and Na/(Na+K) ratios low (0.02). Al_{iv} values of 0.94-1.01 are indicative of phengitic white mica compositions.

6. DISCUSSION

6.1 Fluid/rock interaction and active VHMS mineralization at Iheya North

The recovery of massive sphalerite-(pyrite-chalcopyrite±galena)-rich sulfides from below the seafloor at Iheya North represents an extraordinary achievement for the IODP. At site C0016, recovered blocks of sphalerite-rich massive sulfide from the base of North Big Chimney show clear microstructural evidence of formation via a combination of surface detrital and subsurface chemical processes (**Fig. 4c**), with no subsequent deformation as highlighted by EBSD analysis (**Fig. 5**). At least two episodes of sphalerite mineralization have been recognized. Early Fe-poor sphalerite appears to be detrital in origin and occurs as 0.5 mm subhedral, slightly rounded crystals with inclusions of chalcopyrite. This generation is overgrown by pyrite (±galena), and in turn by chalcopyrite (**Fig. 4d**). A second generation of Fe-poor sphalerite most likely occurred as the system cooled, prior to final seawater influx represented by late coarse anhydrite crystals (**Fig. 4b**). This second generation includes colloform- and atoll-textured aggregates (**Fig. 4c**).

Massive sulfides are polymetallic and characterized by high Zn (30.2%), Pb (12.3%) and Cu (2.68%), plus elevated Ag (33.1 ppm) and Sb (25.6 ppm) concentrations. Low Au concentrations (maximum 0.07 ppm) may be a result of phase separation at depth, as indicated by chloride concentrations that are lower than seawater (Chiba et al., 1996) and flashing (rapid boiling) during IODP drilling (Takai et al., 2011). This is consistent with the lower confining pressures from shallower water depths of the middle Okinawa Trough (<1000 m; Chiba, 1997) when compared to the PACMANUS (~1650 m) and DESMOS (~2000 m) systems of the Manus Basin, and similar hydrothermal fields of the Lau Basin (e.g. Valu Fa Ridge, ~1700 m) (Ishibashi and Urabe, 1995).

Altered volcanic rocks at site C0016 beneath massive sulfides exhibit quartz-muscovite/illite and quartz-Mg-chlorite alteration (**Fig. 10**), reminiscent of the proximal footwall alteration typically associated with ancient VHMS deposits (Large et al., 2001a,b; Piercey, 2009). Low concentrations of SiO_2, Al_2O_3, MgO and K_2O in massive sulfides resulted from large mass gains of Fe, S and base metals (**Fig. 8**).

At site C0013, a likely location of recent high temperature discharge, intense hydrothermal alteration obliterates primary mineralogy and texture. Near surface alteration is dominated by kaolinite and muscovite with locally abundant native S, which is indicative of the presence of acidic fluids. The entire sequence grades to Mg-chlorite dominated assemblages at depths of >5 mbsf (**Fig. 10**). Coarse-grained surficial sulfidic sediments at site C0013 contain ~43.2% Zn, 4.4% Pb, 5.4% Cu and 42 ppm Ag, with high concentrations of As, Cd, Mo, Sb and W. These sediments are interpreted to represent collapsed chimney

structures. They contain significantly higher Zn, Cu, Ag, Sb and As concentrations than massive sulfides from hole C0016B.

Distinctive white coarse rounded nodules of anhydrite±dolomite±talc±calcite±quartz± sphalerite±pyrite (**Fig. 3a**) likely precipitated from down welling seawater at an early stage in the evolution of the hydrothermal system (**Fig. 11a**). These anhydrite veins were subsequently reworked during the main phase of hydrothermal activity (**Fig. 11b**). The presence of yellow native sulfur cement in the top of hole C0013E (**Fig. 3c**) indicates that the sediment was infiltrated by liquid native sulfur at temperatures between 112 and 119 °C (Takai et al., 2011). The transition from kaolinite-muscovite to chlorite-rich alteration assemblages with increasing depth (**Fig. 11b**) is similar to the gradation from paragonitized to chloritized rocks below the TAG hydrothermal field. The major difference in mineralogy between these two fields is due to lack of Fe in the system and abundance of K available from the leaching of underlying felsic basement. A zone of coarse-grained crystalline anhydrite that overlaps the kaolinite and Mg-chlorite alteration zones is interpreted to have precipitated from down welling seawater that penetrated the sediments when hydrothermal activity at the site waned (**Fig. 11c**). Volcanic basement at site C0013 consists of hard quartz and Mg-chlorite altered volcanic breccia with scattered quartz-sulfide (sphalerite-pyrite±covellite±native Cu) veining and trace fine disseminated pyrite within clasts.

6.2. Distal hydrothermal alteration, mineralization and system recharge

Site C0014 represents a more distal locality to the main zone of hydrothermal activity, ~450 m from NBC and ~350 m from site C0013 (**Fig. 10**). At site C0014, covellite and sphalerite mineralization is significantly less abundant. Anhydrite is present from ~57 mbsf as mm-scale irregular veinlets, but is in much lower abundance than at proximal site C0013. Pyrite occurs only in trace amounts and is rarely present as coarser veins. Mg-chlorite alteration occurs from ~30 mbsf, at much greater depths than sites C0016 and C0013. Higher Na_2O concentrations at site C0014 and lower Sb contents than site C0013 are consistent with the more distal location of site C0014 (e.g. Large et al., 2001b; Piercey, 2009).

Recovered lithologies from distal sites C0015 and C0017 are unaltered, with low MgO, Fe_2O_3, LOI, CCPI, AI, base metal concentrations and VHMS 'pathfinder' elements (e.g. Sb, Sn, Cd, Tl; Large et al., 2001b; Piercey, 2009). Downhole temperature profiles at C0017 are also indicative of lateral fluid flow recharge into the system approximately 1.6 km east of NBC (Takai et al., 2011). Site C0015 is interpreted to represent a background locality where porous strata are saturated with seawater.

6.3. A modern analogue for Kuroko-type VHMS mineralization

Recent interest surrounding the potential to mine modern seafloor massive sulfide (SMS) deposits, such as the Solwara 1 deposit of the Manus Basin (Golder Associates, 2012; Yeats, 2012), has highlighted the importance of identifying robust modern analogues for different styles of VHMS mineralization. For instance, the Cu-Zn rich TAG site, a sediment-starved system on the Mid Atlantic Ridge (e.g. ODP Expedition 158), has been compared to Cyprus-type VHMS deposits (Hannington et al., 1998). IODP Expedition 331 was the first time an active hydrothermal system in a continental back-arc setting has been drilled by the ODP / IODP (Takai et al., 2011, 2012). VHMS deposits which form in these settings fall into the Kuroko-type class (Barrie and Hannington, 1999; Galley et al., 2007; Piercey, 2011).

Kuroko-type VHMS deposits are typically polymetallic (Zn-Pb-Cu-Ag-Au), of high grade (Piercey, 2007), and hosted in bimodal felsic flow-dominated sequences where felsic rocks are in greater abundance than mafic rocks and there are less than 15% of siliciclastic rocks in the host succession (Galley et al., 2007; Piercey, 2011). On idealized cross sections, Kuroko-type VHMS deposits are developed on felsic flow complexes, such as rhyolite domes with associated tuffs and breccias (Franklin, 1981). Eight zones of massive/semi-massive mineralization were recognized by Eldridge et al. (1983) which may be present, and three zones associated with the underlying chloritic stockwork. In descending order from the top of the deposit the massive zones are: i) tetsusekiei (quartz-hematite±barite±sulfide), ii) barite ore (barite>sulfide), iii) massive black ore (sphalerite±barite>pyrite-galena>tetrahedrite); iv) semi-massive black ore (sphalerite±barite>pyrite>chalcopyrite-quartz), v) massive yellow ore (chalcopyrite-pyrite>quartz); vi) powdery yellow ore (pyrite>chalcopyrite); vii) massive pyrite ore (pyrite>>chalcopyrite>>sphalerite), and viii) massive gypsum-anhydrite ore (Ca sulfates>>sulfides). These zonations typically occur within a broadly stratiform mound, with the first seven forming imperfectly concentric shells, often with gradational contacts (unless reworked) (Eldridge et al., 1983). An underlying discordant zone of siliceous ore is often associated with the underlying chloritic stockwork with a general zonation from yellow ore (quartz>pyrite>chalcopyrite) in the middle, toward a more sphalerite-galena rich mineral assemblage at the base of the overlying lens, and a quartz>pyrite>>chalcopyrite mineralogy at depth (Eldridge et al., 1983). Classic examples of Kuroko-type VHMS deposits are found in the Honshu arc of Japan in the Hokuroku district, with deposit clusters associated with back-arc rifting (Yamada and Yoshida, 2011), the Mount Read volcanic belt of SE Australia

(Large et al., 2001b), Buchans Group of Newfoundland (Piercey et al., 2007), and Skellefte distict of northern Sweden (Allen et al., 1996).

At Iheya North, massive sulfides intercepted at the base of North Big Chimney strongly resemble the black ore of the Miocene-age Kuroko deposits of Japan (Sato, 1974, 1977), with equivalents to the yellow, gypsum and siliceous ores also recogized by Ishibashi et al. (2013). Massive sulfides are polymetallic and characterized by high Zn (30.2%), Pb (12.3%) and Cu (2.68%), and elevated Ag (33.1 ppm) and Sb (25.6 ppm) concentrations. These metal concentrations are consistent with massive sulfides from Kuroko-type VHMS deposits worldwide (e.g. Barrie and Hannington, 1999; Galley et al., 2007; Large et al., 2001b; Piercey, 2007, 2009), in addition to the increased abundance of pyrite with respect to sphalerite at depth - both on the local scale within the massive sulfide and overall in the sequence (e.g. Sato, 1977; Eldridge et al., 1983). This is also reflected by higher Fe/Zn ratios with depth at site C0016. The clastic nature of the massive and semi-massive sulfides at site C0016 is also consistent with observations from the Kuroko deposits of Japan (e.g. Kuroda, 1977; Eldridge et al., 1983).

The quartz-Mg-chlorite basement present at sites C0016, C0013 and C0014 is typical of high-temperature hydrothermal alteration associated with VHMS systems (Galley et al., 2007; Piercey, 2009). All rocks analysed from C0016 show large gains in SiO_2 and MgO, with the latter increasing downhole (**Fig. 8**). It is important to note the reduced depth of the Mg-chlorite alteration towards NBC - from ~30 mbsf at site C0014 to ~6 mbsf at site C0013 (**Fig. 10**). Aoyama et al. (2014) highlight that this zone at site C0014 corresponds with shifts in Mg, K and SO_4 pore water chemistry and $\delta^{34}S$ values. Whereas the unaltered sediment at site C0014 (**Fig 2b**) is saturated with seawater, the Mg-chlorite altered zone is dominated by hydrothermal fluid and has yielded significantly higher temperatures (Takai et al., 2011). Bacteriogenic sulfate reduction is only evident in the unaltered sediments (Aoyama et al., 2014).

Decreasing Na_2O concentrations in felsic volcanic and volcaniclastic rocks at Iheya North with proximity to NBC is consistent with observations from ancient Kuroko-type VHMS deposits (Date et al., 1983; Hashiguchi et al., 1983; Piercey, 2009). For example, Date et al. (1983) recognized a Na_2O-depleted dacite mass with the lateral dimensions of 1.5 by 3 km immediately below the ore horizon associated with the Fukazawa deposits. This was interpreted to reflect feldspar destruction and sericite formation at relatively low pH and high temperatures. It was hypothesised that much of the sodium lost from footwall lithologies was added to the rocks in zones I (distal; forming analcime) and IV (proximal; forming Na-

montmorillonite in the hanging-wall). In the Miocene footwall rocks of the Uwamuki deposits, Urabe et al. (1983) noted a mineralogical zonation from core to margin of quartz-sericite, sericite-chlorite-quartz, remnant albite-sericite-chlorite-quartz and kaolinite-quartz-sericite-chlorite±albite.

Recovered footwall felsic volcanic rocks from site C0016 (and elsewhere) are of FII to FIII affinity with well-developed negative Eu anomalies, similar to felsic volcanic rocks hosting ancient Kuroko-type VHMS deposits that formed in Phanerozoic ensialic back-arc settings worldwide (e.g. Leat et al., 1986; McConnell et al., 1991; Piercey, 2011). In some instances the period of VHMS mineralization may be associated with a shift in immobile element characteristics of the host lithologies (i.e. higher HFSE concentrations in pre-ore felsic rocks; Yamada and Yoshida, 2011). However, this features has also been observed in bimodal-mafic or Noranda-type VHMS systems (e.g. Golden Grove & Teutonic Bore; Hollis et al., 2015).

Chlorite analyses from site C0016 plot consistently within the Mg-rich clinochlore and penninite fields (**Fig. 9**). These compositions are similar to chlorite associated with the SE Australian Kuroko-type VHMS deposits such as Thalanga, and some analyses of footwall chlorite at Hellyer (**Fig. 9**). Fe/Fe+Mg ratios from Iheya North are significantly lower than values reported at other active hydrothermal fields such as TAG and PACMANUS, plus Noranda-type (i.e. bimodal-mafic) VHMS deposits (e.g. Noranda belt, Mattagami Lake; **Fig. 9**). Work by McLeod and Stanton (1984) on the SE Australian Kuroko-type VHMS deposits (e.g. Woodlawn, Que River) observed that chlorite associated with sphalerite-rich ore had significantly lower Fe/Fe+Mg ratios than chalcopyrite-rich samples. This is entirely consistent with chlorite geothermometers which utilise Fe/Fe+Mg ratios (e.g. MacLean and Kranidotis, 1987), as higher temperatures would be expected for chalcopyrite precipitation. Fe-poor sphalerite and Mg-rich chlorite compositions at Iheya North are consistent with the overall low Fe-budget of the system, and Zn-rich nature of the mineralization.

Chlorite geothermometers which utilise Fe/Fe+Mg ratios (MacLean and Kranidotis, 1987; Zhang and Fyfe, 1995) yield average temperature estimates of 218-235 °C for sphalerite-rich massive sulfides and 225-241 °C for quartz-chlorite altered volcanic rocks characterized by higher Cu/Fe and Cu/Zn ratios. These temperatures are consistent with hydrothermal fluids associated with Kuroko-type VHMS mineralization (e.g. Kalogeropoulos and Scott, 1983; Shikazono et al., 1983), with temperatures of >250 ˚C when associated with chalcopyrite. EBSD data also reveal higher temperature microstructures downhole at site

C0016, and temperature induced grain boundary migration through more lobate HAGBs (e.g. 16B-3B, **Fig. 5l**).

6.4. Role of sediments on fluid flow and chemistry

Although there is less interaction between hydrothermal fluids and sediments at Iheya North than the JADE and CLAM sites of the middle Okinawa Trough (Glasby and Notsu, 2003), high alkalinity, NH_4^+, CH_4 and CO_2 at Iheya North are still indicative of some reaction with organic matter. Anomalously high alkalinity and NH_4^+ at the CLAM site of the middle Okinawa Trough, coupled with significantly higher $\delta^{34}S$ of sulfate than ambient seawater indicate that sulfate reduction plays a dominant role in decomposing organic material (see Glasby and Notsu, 2003). Oxidation of significant quantities of H_2S in organic matter at Iheya North, evident from the local presence of native S, coupled with Mg-fixation in chlorite ultimately resulted in the stabilization of the potassic alteration assemblages observed during IODP Expedition 331. Sediment input has also previously been used to explain higher concentrations of Pb (13.5%), Zn (31.4%), Sb (1,140 ppm), As (1,730 ppm) and Ag (465 ppm) in chimney samples from Iheya North (average values from Ueno et al., 2003) than in Kuroko-type deposits (Glasby and Notsu, 2003). Lead in the JADE deposits is derived from both sediments and volcanic rocks (Halbach et al., 1997; Zeng et al. 2000), similar to the Kuroko-type VHMS deposits of Japan (Fehn et al., 1983). For comparison, the influence of sediment in mafic dominated hydrothermal systems is provided by ODP legs to the un-sedimented TAG VHMS mound and the sedimented Middle Valley (summarized by Shanks, 2012).

More recent work by Keith et al. (2014) has linked Fe/Zn ratios in sphalerite to the influence of fS_2 and fO_2 on Fe partitioning between fluids and sphalerite. It was stated that sphalerite from sediment-hosted vents has systematically higher S concentrations and Fe/Zn ratios than those of the sediment-starved vents. This is again consistent with data presented by Ishibashi et al. (2015) from the middle Okinawa Trough. Whereas the Iheya North, Yoron, Minami-Ensei, Irabu and Hatoma fields are characterized by low Fe/Zn ratios in sphalerite (FeS typically <5 mol %), data from the more sedimented JADE and Yonaguni IV fields progressed to considerably higher values (Ishibashi et al., 2015). The CLAM site in particular is characterized by a thick blanket of muddy sediments, with associated Zn-mineralization dominated by wurtzite (Glasby and Notsu, 2003). Proton-induced X-ray emission mapping has confirmed the Fe-poor nature of the sphalerite from site C0016 massive sulfides, plus an association between sphalerite and high Cd (Yeats & Laird, unpublished).

As impermeable hemipelagic sediments are interlayered with volcaniclastic sediments through the upper part of the Iheya North stratigraphy (**Fig. 2**), hydrothermal fluids are channelled laterally in porous and permeable volcaniclastic units, and vertically predominantly through faults (Takai et al., 2011; **Fig. 10**). Locally sourced woody pumice and pumiceous pyroclastic flow deposits have been recovered by numerous gravity cores obtained from the central valley of Iheya North Knoll (Oiwane et al., 2008). In all cores, thick pumice layers with coarse to fine grain sizes were found just below the seafloor. These layers often contain abundant gas-filled voids accompanied by elemental sulphur and sulfide minerals, deposited by a gas-rich hydrothermal fluid (Oiwane et al., 2008). Shipboard pore-water chemistry also shows clear evidence for the compartmentalization of hydrothermal fluids due to the presence of thick sequences of hemipelagic sediment (Takai et al., 2011).

7. CONCLUSIONS

The mineralization and alteration assemblages intercepted during IODP Expedition 331 at Iheya North provide a relatively complete (though fragmental) profile through a developing Kuroko-type VHMS system. At site C0016, located adjacent to the foot of the actively venting NBC massive sulfide mound, massive sphalerite-(pyrite-chalcopyrite±galena)-rich sulfides were recovered that strongly resemble the black ore of the Miocene-age Kuroko deposits of Japan. Sulfide mineralization shows clear evidence of formation through a combination of surface detrital and subsurface chemical processes, with at least some sphalerite precipitating into void space in the rock. Underlying volcanic rocks exhibit quartz-muscovite/illite and quartz-Mg-chlorite alteration reminiscent of VHMS proximal footwall hydrothermal alteration.

Site C0013, ~100 m east of NBC, represents a likely location of recent high temperature discharge, with surficial coarse-grained sulfidic sediments containing high concentrations of As, Mo, Sb and W. Near surface alteration is dominated by kaolinite and muscovite with locally abundant native sulfur, indicative of acidic fluids, grading to Mg-chlorite dominated assemblages at depths of >5 mbsf. Late coarse-grained anhydrite veining overprints earlier alteration and is interpreted to have precipitated from down welling seawater as hydrothermal activity waned. At site C0014, ~150 m farther east, hydrothermal assemblages are characterized by illite/montmorillonite, with Mg-chlorite present at ~30 mbsf. Recovered lithologies from distal, recharge site C0017 are unaltered.

The metal tenors and alteration assemblages at Iheya North are significantly different from those observed at deposits hosted in Mid Ocean Ridge (Cyprus-type) and primitive arc

(e.g. Noranda-type) environments. Mineralization and alteration assemblages are consistent with the Iheya North system representing a modern analogue for Kuroko-type VHMS mineralization. Fluid flow is focussed laterally along pumiceous volcaniclastic strata (compartmentalized between impermeable hemipelagic sediments), and vertically along faults.

ACKNOWLEDGEMENTS

The authors thank the crew of R/V Chikyu during IODP Expedition 331, particularly co-chief scientists Ken Takai and Mike Mottl. Junichiro Ishibashi, Stephen Bowden and Yuka Masaki are thanked for thoughtful on-board discussions. Costs associated with Chris Yeats', Steven Hollis', Juan Carlos Corona's and Gordon Southam's participation in IODP Expedition 331 were supported by the Australia-New Zealand IODP Consortium, IODP UK, the U.S. Science Support Program, and the National Sciences and Engineering Research Council of Canada, respectively. Steven Hollis is currently supported by the Irish Centre for Research in Applied Geosciences (iCRAG) through funding from Science Foundation Ireland (SFI). Financial support for Angela Halfpenny was provided the Commonwealth Scientific and Industrial Research Organisation's (CSIRO), Office of the Chief Executive (OCE) postdoctoral research funding scheme. Stephen Barnes (CSIRO) is thanked for funding whole rock geochemistry. The authors thank the Integrated Ocean Drilling Program for the opportunity to sail and access to samples. Marco Fiorentini acknowledges support from the Australian Research Council through Linkage Project LP120100668, the Future Fellowship Scheme (FT110100241), and the ARC Centre for Excellence for Core to Crust Fluid Systems (CE11E0070). Crystal LaFlamme acknowledges support from the Minerals Research Institute of Western Australia and Science and Industry Endowment Fund and Geological Survey of Western Australia. This manuscript was greatly improved by constructive comments from editor Franco Pirajno and two anonymous reviewers. This is contribution *** from the ARC Centre for Excellence for Core to Crust Fluid Systems.

LIST OF FIGURES

Figure 1. (a) Geological Setting of the Iheya North hydrothermal field of the middle Okinawa Trough, Japan (modified after Ishibashi et al., 2015; Shinjo & Kato, 2000). **(b-c)** Bathymetric maps of the Iheya North hydrothermal field and IODP Expedition 331 drill sites (after Ishibashi et al., 2015; Takai et al., 2011). NBC, North Big Chimney.

Figure 2. Sedimentary logs for the deepest holes at sites C0013 and C0014 with alteration assemblages determined by shipboard XRD indicated. **(a)** Hole C0013E. **(b)** Hole C0014G.

Figure 3. Key lithologies recovered from sites C0013 **(a-e)** and C0016 **(f-j)**. All core recovered from site C0016 is shown. **(a)** Mottled Mg-chlorite and anhydrite alteration in sediments from hole C0013D. Note the large white nodules of anhydrite with truncated internal structures, indicating physical or chemical erosion after precipitation. **(b)** Quartz and Mg-chlorite altered volcanic basement with stockwork veining (site C0013E) containing sphalerite, pyrite and covellite. **(c)** Native sulfur bearing sediment at the top of hole C0013E. As the sulfur occurs as veinlets and cements this implies it was liquid when the interval formed. **(d)** Native S crystalline linings on gaseous or fluid filled voids in silty mud from hole C0013F. **(e)** Native Cu (confirmed by SEM) and organic carbon present in volcanic basement at depth from site C0013E. **(f)** Blocks of hard clastic massive/semi-massive sulfide dominated by sphalerite from C0016B (labelled 1-3; from 0-9 mbsf). **(g)** Silicified volcanic with sulfide veining (labelled 4) recovered from the core catcher from 0-9 mbsf. **(h)** Lithologies recovered from between 9 and 27 mbsf: silicified volcanic rock (labelled 5), a coarsely crystalline anhydrite aggregate with sulfide veining (labelled 6) and quartz-clay altered volcanic breccia (labelled 7). **(i)** Quartz-chlorite altered volcanic rock recovered from between 27-45 mbsf, which displays a network of quartz-chlorite-pyrite veins. **(j)** Quartz-chlorite-pyrite veining cut by a later anastomosing pyrite-anhydrite vein network, in quartz-chlorite altered volcanic basement (recovered from the core catcher; from 27-45 mbsf).

Figure 4. Petrographic and backscattered SEM photomicrographs of samples recovered from Iheya North. **(a)** Massive sulfide from site C0016B showing intergrown pyrite-chalcopyrite-sphalerite-galena (reflected light). Chalcopyrite has overgrown pyrite, with sphalerite showing chalcopyrite disease. **(b)** Coarsely crystalline anhydrite overgrowing quartz and sulfide in sphalerite-rich massive sulfides from site C0016B. **(c)** Colloform/atoll textured sphalerite overgrowing pyrite and chalcopyrite in massive sulfides at site C0016B (reflected light). **(d)** Silicified volcanic rock underlying massive sulfides at site C0016B (reflected light). Sphalerite is overgrown by galena, and in turn by pyrite and chalcopyrite. **(e)** Covellite present in sulfidic sediments from site C0013 (image taken under binocular microscope). **(f)** SEM image of euhedral covellite from sulfidic sediment (near surface) at C0013E. **(g)** Euhedral and framboidal pyrite present in sulfidic sediments at site C0013 (image taken under binocular microscope). **(h)** SEM

photomicrograph of framboidal pyrite aggregates from sulfidic sediment (near surface) C0013C. **(i)** SEM photomicrograph showing the hydration of anhydrite to gypsum during dissolution at site C0013B. **(j)** SEM photomicrograph of opaline silica with silver arsenide (bright white material) from site C0013B. **(k)** Euhedral pyrite intergrowths in clay from C0014G **(l)** SEM photomicrograph of a polymetallic sulfide vein from site C0014G with intergrown sphalerite, chalcopyrite and galena.

Figure 5. (a, d, g, j, m) Reflected light photomicrographs of the areas analysed by coincident EDS/EBSD. **(b, e, h, k, n)** phase maps created from EDS data (sphalerite = dark blue, quartz = red, pyrite = orange, chalcopyrite = lime green, chlorite = aqua blue, graphite = grey, anhydrite = pink). **(c, f, i, l, o)** EBSD data plotting the phases (sphalerite = blue, quartz = red, pyrite = orange, chalcopyrite = lime green) overlain on the pattern quality map, with high angle grain boundaries (HAGB) in black, low angle grain boundaries (LAGB) in white, and sigma 3 coincident site lattices (CSL) in red. *Samples:* **Figure 5a-f:** sphalerite-rich semi-massive sulfide (C0016B, block 2 in **Figure 3f**). **Figure 5g-l:** sphalerite rich semi-massive sulfide (C0016B, block 3 in **Figure 3f**). **Figure 5m-o** quartz and Mg-chlorite altered volcanic rock with stringer sulfides (C0016B, block 9 in **Figure 3j**)

Figure 6. Whole rock geochemical variation at Iheya North. **(a)** Pearce (1996) whole rock Zr/TiO_2 vs. Nb/Y discrimination diagram for the classification of hydrothermally altered volcanic and volcaniclastic rocks. All samples plot within the felsic (rhyolite/dacite) field except for 5 samples which contain significant quantities of hemipelagic/hydrothermal clay (IN08 and IN19-20 respectively) or are strongly mineralized (IN01). **(b)** Alteration Box Plot of major element mobility (after Large et al. 2001a). CCPI (Chlorite-Carbonate-Pyrite Index) = 100 (MgO + FeO) / (MgO + FeO + Na_2O + K_2O). AI (Ishikawa Alteration Index) = 100 (K_2O + MgO) / (K_2O + MgO + Na_2O + CaO). The Ishikawa Alteration Index quantifies the intensity of sericite and chlorite alteration that occurs in footwall rocks proximal to Kuroko-type VHMS deposits. High AI is associated with the breakdown of sodic plagioclase and volcanic glass and their replacement by sericite and chlorite. The Chlorite-Carbonate-Pyrite Index quantifies increases in MgO and FeO associated with Mg-Fe chlorite development, which commonly replaces albite, K feldspar or sericite. It also is affected by Mg-Fe carbonate alteration, and enrichments in pyrite, magnetite and hematite. Mineral nodes and common alteration trends associated with hydrothermal alteration are shown. **(c)** Zr/Y vs. Y fertility plot of Lesher et al. (1986) for the VHMS

prospectivity of felsic rocks. Inset image shows the La/Yb_{CN} vs. Yb_{CN} fertility plot of Hart et al. (2004). Samples analysed from Iheya North are predominantly of FII to FIIIa affinity and similar to VHMS associated felsic rocks in ensialic arc settings worldwide. **(d)** Nb vs. Y diagram highlighting the HFSE enrichment of the least altered felsic rocks at Iheya North. Large mass gains of mobile elements (e.g. Fe, S, Si, Mg, Zn) result in the dilution of Nb and Y while maintaining immobile-element ratios. **(e)** Chondrite normalized REE diagram illustrating the slight LREE enrichment, flattish HREE profiles and pronounced negative Eu anomalies for most samples. Chondrite normalization values from McDonough and Sun, 1995).

Figure 7. Isocon diagrams for representative samples from Iheya North (after the method of Grant, 1986, 2004). Isocons were fitted using a range of immobile elements (shown in red). Element concentrations are scaled for plotting convenience using the values listed in Table 2. **(a)** IN01, sphalerite-rich massive sulfide from site C0016 (see **Figure 3a**). **(b)** IN02, silicified volcanic rock with disseminated sulfides from site C0016 that underlies massive and semi-massive sulfide (see **Figure 3f**). **(c)** IN05, quartz-Mg-chlorite altered volcanic rock with stringer sulfides from site C0016 (see **Figure 3h**). **(d)** IN15, quartz-chlorite altered volcanic rock from depth at site C0013. **(e)** IN09, unaltered pumice with trace oxidized yellow clay staining from site C0015. **(f)** Schematic cartoon for the interpretation of isochon diagrams.

Figure 8. Calculated mass change values for selected samples from sites Iheya North after Grant (1986, 2004). Mass change was calculated using the immobile element isocons and equations in **Figure 7**. Large mass gains of Zn-Pb-Cu-Fe-S occur in IN01. Underlying silicified (IN02) and quartz-chlorite altered volcanic rocks also show large gains in Si±Mg, whereas samples from C0013 (IN15) and C0015 (IN09) show significantly reduced mass gains.

Figure 9. Chlorite chemistry for samples analysed from hole C0016B compared to other active hydrothermal systems and ancient VHMS deposits. Data compiled from: Arctic VHMS deposit, Alaska (Schmidt 1988), Heath Steel B Zone VHMS deposit, New Brunswick, Canada (Lentz et al., 1997), Hellyer VHMS deposit, western Tasmania, Australia (Gemmell and Fulton, 2001), Horne VHMS deposit, Noranda, Quebec (MacLean and Hoy, 1991), Iberian Pyrite belt, SW Spain (Sánchez-España et al., 2000), Mattagami Lake, Quebec, Canada (Costa et al., 1983), PAC-MANUS (Paulick and Bach, 2006), TAG (Sturz et al., 1998), Thalanga VHMS deposit, northern Queensland,

Australia (Paulick et al., 2001), Turkey VMS deposits (Catagay, 1993), Wolverine volcanic-sediment hosted deposit, Finlayson Lake, Canada (Bradshaw et al., 2008).

Figure 10. Schematic cartoon for the Iheya North hydrothermal field.

Figure 11. Schematic model for evolution of hydrothermal activity at site C0013. **(a)** Eroded anhydrite veining/nodules occur within a mixed sequence of felsic volcaniclastic rocks and hemipelagic sediments on an unaltered volcanic basement. **(b)** Hydrothermal activity is associated with the alteration of the volcanic basement to quartz-Mg-chlorite and Mg-chlorite-talc in the overlying sediments, and venting at the seafloor. The uppermost portion of the sedimentary sequence is characterized by a lower temperature assemblage of kaolinite-muscovite, indicative of acidic fluids. **(c)** As hydrothermal activity ceases, cool seawater infiltrates the sediment precipitating coarsely crystalline anhydrite above the 150 °C isotherm. Sulfide chimneys collapse to form occurrences of sulfide-rich sediment, which contain varying base metal concentrations.

REFERENCES

Allen, R.L., Weihed, P., Svensson, S.A., 1996. Setting of Zn-Cu-Au-Ag massive sulphide deposits in the evolution and facies architecture of a 1.9 Ga marine volcanic arc, Skellefte district, Sweden. Economic Geology, 91, 1022-1053.

Aoyama, S., Nishizawa, M., Takai, K., Ueno, Y., 2014. Microbial sulfate reduction within the Iheya North subseafloor hydrothermal system constrained by quadruple sulfur isotopes. Earth and Planetary Science Letters, 398, 113-126.

Barrie, C.T., Hannington, M.D., 1999. Introduction: classification of VMS deposits based on host rock composition, in: Barrie, C.T., Hannington, M.D. (Eds.), Volcanic-associated massive sulfide deposits: processes and examples in modern and ancient settings. Reviews in Economic Geology, 8, 2-10.

Barrie, C.T., Ludden, J.N., Green, T., 1993. Geochemistry of volcanic rocks associated with Cu-Zn and Ni-Cu deposits in the Abitibi Subprovince. Economic Geology, 88, 1341-1358.

Barriga, F., Binns, R., Baldauf, J., Miller, D.J, 2000. Anatomy of an active, felsic-hosted hydrothermal system, eastern Manus Basin. Leg 193 Scientific Prospectus, Ocean Drilling Program, 1-60.

Bradshaw, G.D., Rowins, S.M., Peter, J.M., Taylor, B.E., 2008. Genesis of the Wolverine volcanic sediment-hosted massive sulfide deposit, Finlayson Lake District, Yukon, Canada: mineralogical, mineral chemical, fluid inclusion, and sulfur isotope evidence. Economic Geology, 103, 35-60.

Catagay, M.N., 1993. Hydrothermal alteration associated with volcanogenic massive sulfide deposits: examples from Turkey. Economic Geology, 88, 606-621.

Chiba, H., Ishibashi, J.-I., Ueno, H., Oomori, T., Uchiyama, N., Takeda, T., Takemine, C., Ri, J., Itomitsu, A., 1996. Seafloor hydrothermal systems at North Knoll, Iheya Ridge, Okinawa Trough. JAMSTEC Journal of Deep Sea Research, 12, 211-219. (in Japanese with English Abstract)

Chiba, H., 1997. Geochemistry of active hydrothermal systems in Okinawa Trough back arc basin. JAMSTEC Deep-Sea Research, Special Volume, 63-68.

Connelly, D.P., Copley, J.T., Murton, B.J., Standfield, K., Tyler, P.A., German, C.R., Van Dover, C.L., Amon, D., Furlong, M., Grindlay, N., Hayman, N., Hühnerbach, V., Judge, M., Le Bas, T., McPhial, S., Meier, A., Nakamura, K.-i., Nye, V., Pebody, M., Pedersen, R.B., Plouviez, S., Sands, C., Searle, R.C., Stevenson, P., Taws, S., Wilcox, S., 2012. Hydrothermal vent fields and chemosynthetic biota on the world's deepest seafloor spreading centre. Nature Communications, 3, 620.

Costa, U.R., Barnett, R.L., Kerrich, R., 1983. The Mattagami Lake mine Archean Zn-Cu sulfide deposit, Quebec: hydrothermal coprecipitation of talc and sulfides in a sea-floor brine pool – evidence from geochemistry, $^{18}O/^{16}O$, and mineral chemistry. Economic Geology, 78, 1144-1203.

Date, J., Watanabe, Y., Saeki, Y., 1983. Zonal alteration around the Fukazawa Kuroko deposits, Akita Prefecture, northern Japan. In: Ohmoto, H., Skinner, B.J. (eds.) Kuroko and related volcanogenic massive sulfide deposits. Economic Geology, Monograph 5, 365-386.

de Ronde, C.E.J., Faure, K., Bray, C.J., Chappell, D.A., Wright, I.C., 2003. Hydrothermal fluids associated with seafloor mineralization at two southern Kermadec arc volcanoes, offshore New Zealand. Mineralium Deposita, 38, 217-233.

de Ronde, C.E.J., Hannington, M.D., Stoffers, P., Wright, I.C., Ditchburn, R.G., Reyes, A.G., Ishibashi, J., Lebon, G.T., Bray, C.J., Resing, J.A., 2005. Evolution of a submarine magmatic-hydrothermal system: Brothers volcano, southern Kermadec arc, New Zealand. Economic Geology, 100, 1097-1133.

Eldridge, C.S., Barton Jr, P.B., Ohmoto, H., 1983. Mineral textures and their bearing on the formation of Kuroko orebodies. In: Ohmoto, H., Skinner, B.J. (eds.) Kuroko and related volcanogenic massive sulfide deposits. Economic Geology, Monograph 5, 241-281.

Fehn, U., Doe, B.R., Delevaux, M.H., 1983. The distribution of lead isotopes and the origin of Kuroko ore deposits in the Hokuroku district, Japan. Economic Geology Monograph 4, 488-506.

Fougerouse, D., Micklethwaite, S., Halfpenny, A., Reddy, S.M., Cliff, J.B., Martin, L.A.J., Kilburn, M., Guagliardo, P., Ulrich, S., 2016a. The golden ark: Arsenopyrite crystal plasticity and the retention of gold through high strain and metamorphism. Terra Nova, 28, 181-187.

Fougerouse, D., Micklethwaimte, S., Tomkins, A.G., Mei, Y., Kilburn, M., Guagliardo, P., Fisher, L.A., Halfpenny, A., Gee, M., Paterson, D., Howard, D.L., 2016b. Gold remobilisation and formation of high grade ore shoots driven by dissolution-reprecipitation replacement and Ni substitution into auriferous arsenopyrite. Geochimica et Cosmochimica Acta, 178, 143-159.

Fouquet, Y., Zierenberg, R., Miller, J., the Leg 169 Scientific Party, 1997. Leg 169 drills a major massive sulfide deposit on a sediment-buried spreading center. JOIDES Journal, 23, 4–5.

Franklin, J.M., Sangster, D.F., Lydon, J.W., 1981. Volcanic-associated massive sulfide deposits. Economic Geology, 75th Anniversary Volume, 485-627.

Franklin, J.M., Gibson, H.L., Galley, A.G., Jonasson, I.R., 2005. Volcanogenic massive sulfide deposits, in: Hedenquist, J.W., Thompson, J.F.H., Goldfarb, R.J., Richards, J.P. (Eds.), Economic Geology 100th Anniversary Volume. Society of Economic Geologists, 523-560.

Galley, A.G., Bailes, A.H., Kitzler, G., 1993. Geological setting and hydrothermal evolution of the Chisel Lake and North Chisel Zn-Pb-Cu-Ag-Au massive sulfide deposits, Snow Lake, Manitoba. Exploration and Mining Geology, 2, 271-295.

Gemmell, J.B., Fulton, R., 2001. Geology, genesis, and exploration implications of the footwall and hanging-wall alteration associated with the Hellyer volcanic-hosted massive sulfide deposit, Tasmania, Australia. Economic Geology, 96, 1003-1035.

Glasby, G.P., Lizasa, K., Hannington, M., Kubota, H., Notsu, K., 2008. Mineralogy and composition of Kuroko deposits from northeastern Honshu and their possible modern analogues from the Izu-Ogasawara (Bonin) Arc south of Japan: implications for mode of formation. Ore Geology Reviews, 34, 547-560.

Glasby, G.P., Notsu, K., 2003. Submarine hydrothermal mineralization in the Okinawa Trough, SW of Japan: an overview. Ore Geology Reviews, 23, 209-339.

Golder Associates., 2012. Mineral resource estimate, Solwara project, Bismark Sea, PNG: technical report compiled under NI43-10, no SL01-NSG-RPT-7020-001 Rev 1, March 23, 2012, 218p.

Grant, J.A., 1986. The Isocon diagram – a simple solution to Gresens Equation for metasomatic alteration. Economic Geology, 81, 1976-1982.

Grant, J.A., 2005. Isocon analysis: a brief review of the method and applications. Physics and Chemistry of the Earth, 30, 997-1004.

Halbach, P., Pracejus, B., Märten, A., 1993. Geology and mineralogy of massive sulfide ores from the Central Okinawa Trough, Japan. Economic Geology, 88, 2210-2225.

Halbach, P., Hansmann, W., Köppel, V., Pracejus, B., 1997. Whole-rock and sulfide lead-isotope data from the hydrothermal JADE field in the Okinawa back-arc trough. Mineralium Deposita, 32, 70-78.

Halfpenny, A., 2010. Some important practical issues for collection and manipulation of electron backscatter diffraction (EBSD) data from rocks and minerals. J. Vir. Exp. 35, 1-18.

Halfpenny, A., 2011. Application of EBSD to Oceanic Gabbros: Insights into an Oceanic Core complex, Australian Microscopy & Microanalysis Newsletter, 42-44.

Halfpenny, A., Hough, R.M., Verrall, M., 2013. Preparation of samples with both hard and soft phases for electron backscatter diffraction: Examples from gold mineralization. Microsc. Microanal. 19, 1007-1018.

Halfpenny, A., Prior, D.J., 2009. An electron backscatter diffraction study of a gabbroic shear zone, IODP Expedition 304/305. In: Blackman, D.K., Ildefonse, B., John, B.E., Ohara, Y., Miller, D.J., MacLoed, C.J. and the Expedition 304/305 Scientists. Proc. IODP, 304/305: College Station Tx.

Halfpenny, A., Prior D.J., Wheeler, J., 2006. Analysis of dynamic recrystallization and nucleation in a quartzite mylonite. Tectonophysics, 427, 3-14.

Halfpenny, A., Prior, D.J., Wheeler, J., 2012. Electron backscatter diffraction analysis to determine the mechanisms that operated during dynamic recrystallisation of quartz-rich rocks. Journal of Structural Geology, 36, 2-15.

Hannington, M.D., Galley, A.G., Herzig, P.M., Petersen, S., 1998. Comparison of the TAG mound and stockwork complex with Cyprus-type massive sulfide deposits, in: Herzig, P.M., Humphris, S.E., Miller, D.J., Zierenberg, R.A. (Eds.) Proceedings of the Ocean Drilling Program, Scientific Results, Vol. 158, 389-415.

Hashiguchi, H., Yamada, R., Inoue, T., 1983. Practical application of low Na_2O anomalies in the footwall acid lava for delimiting promising areas around the Kosaka and Fukazawa Kuroko deposits, Akita Prefecture, Japan. In: Ohmoto, H., Skinner, B.J. (eds.) Kuroko and related volcanogenic massive sulfide deposits. Economic Geology, Monograph 5, 387-394.

Humphris, S.E., Alt, J.C., Teagle, D.A.H., Honnorez, J.J., 1998. Geochemical changes during hydrothermal alteration of basement in the stockwork beneath the TAG active hydrothermal mound, in: Humphris, S.E., Herzig, P.M., Miller, D.J., Zierenberg, R. (Eds.) Proceedings of ODP Scientific Results, 158, College Station, TX (Ocean Drilling Program), 255-276.

Hart, T.R., Gibson, H.L., Lesher, C.M., 2004. Trace element geochemistry and petrogenesis of felsic volcanic rocks associated with volcanogenic massive Cu-Zn-Pb sulfide deposits. Economic Geology, 99, 1003-1013.

Herrington, R., Maslennikov, V., Zaykov, V., Seravkin, I., Kosarev, A., Buschmann, B, Orgeval, J.-J., Holland, N., Tessalina, S., Nimis, P., Armstrong, R., 2005. Classification of VMS deposits: lessons from the South Uralides. Ore Geology Reviews, 27, 203-237.

Hollis, S.P., Yeats, C.J., Wyche, S., Barnes, S.J., Ivanic, T.J., Belford, S.M., Davidson, G.J., Roache, A.J., Wingate, M.T.D., 2015. A review of volcanic-hosted massive sulfide (VHMS) mineralization in the Archaean Yilgarn Craton, Western Australia: tectonic, stratigraphic and geochemical associations. Precambrian Research, 260, 113-135.

Humpris, S.E., Herzig, P.M., Miller, D.J., Alt, J.C., Becker, K., Brown, D., Brügmann, G., Chiba, H., Fouquet, Y., Gemmell, J.B., Guertin, G., Hannington, M.D., Holm, N.G., Honnorez, J.J., Itturino, G.J., Knott, R., Ludwig, R., Nakamura, J., Petersen, S., Reysenback, A.-L., Rona, P.A., Smith, S., Sturz, A.A., Tivey, M.K., Zhao, X., 1995. The internal structure of an active sea-floor massive sulphide deposit. Nature, 377, 713-716.

Ishibashi, J.-I., Ikegami, F., Tsuji, T., Urabe, T., 2015. Hydrothermal activity in the Okinawa Trough back-arc basin: geological background and hydrothermal mineralization, in: Ishibashi, J.-i. et al (Eds). Subseafloor Biosphere Linked to Hydrothermal Systems: TAIGA Concept. pp337-359.

Ishibashi, J.-I., Miyoshi, Y., Inoue, H., Yeats, C., Hollis, S.P., Corona, J.C., Bowden, S., Yang, S., Southam, G., Masaki, Y., Hartnett, H., IODP Expedition 331 Scientists, 2013. Subseafloor structure of a submarine hydrothermal system within volcaniclastic sediments: a modern analogue for 'Kuroko-type' VMS deposits. In: Mineral Deposit Research for a high-tech world. 12th SGA Biennial Meeting 2013, Proceedings volume 2, 542-544.

Ishibashi, J.-I., Urabe, T., 1995. Hydrothermal activity related to arc-backarc magmatism in the Western Pacific, in: Taylor, B. (Ed.), Backarc Basins: Tectonics and Magmatism. Plenum Press, New York, pp451-495.

Ishizuka, H., Kawanobe, Y., Sakai, H., 1990. Petrology and geochemistry of volcanic rocks dredged from the Okinawa Trough, an active back-arc basin. Geochemical Journal, 24, 75-92.

Jenner, G.A., 1996. Trace element geochemistry of igneous rocks: geochemical nomenclature and analytical geochemistry, in: Wyman, D.A. (Ed.), Trace element geochemistry of volcanic rocks: applications for massive sulfide exploration. Geological Association of Canada, Short Course Notes, 12, 51-77.

Kawagucci, S., Chiba, H., Ishibashi, J.-i., Yamanaka, T., Toki, T., Muramatsu, Y., Ueno, Y., Makabe, A., Inoue, K., Yoshida, N., Nakagawa, S., Nunoura, T., Takai, K., Takahata, N., Sano, Y., Narita, T., Teranishi, G., Obata, H., Gamo., T., 2011. Hydrothermal fluid geochemistry at the Iheya North field in the mid-Okinawa

Trough: implication for origin of methane in subseafloor fluid circulation systems. Geochemical Journal, 45, 109-124.

Kawagucci, S., Miyazaki, J., Nakajima, R., Nozaki T., Takaya, Y., Kato, Y., Shibuya, T., Konno, Y., Nakaguchi, Y., Hatada, K., Hirayama, H., Fujikura, K., Furushima, Y., Yamamoto, H., Watsuji, T., Ishibashi, J-I., Takai, K., 2013. Post-drilling changes in fluid discharge pattern, mineral deposition, and fluid chemistry in the Iheya North hydrothermal field, Okinawa Trough. Geochemistry, Geophysics, Geosystems, 14, 4774-4790.

Kalogeropoulos, S.I., Scott, S.D., 1983. Mineralogy and geochemistry of tuffaceous exhalates (tetusekiei) of the Fukazawa mine, Hokuroko district, Japan. In: Ohmoto, H., Skinner, B.J. (eds.) Kuroko and related volcanogenic massive sulfide deposits. Economic Geology, Monograph 5, 412-432.

Keith, M., Haase, K.M., Schwarz-Schampera, U., Klemd, R., Petersen, S., Back, W., 2014. Effects of temperature, sulphur, and oxygen fugacity on the composition of sphalerite from submarine hydrothermal vents. Geology. First Published online June 30.2014. Doi:10.1130/G35655.1

Klingelhoefer, F., Lee, C.-S., Lin, J.-Y., Sibuet, J.-C., 2009. Structure of the southernmost Okinawa Trough from reflection and wide-angle seismic data. Tectonophysics, 466, 281-288.

Kuroda, H., 1977. Mechanism of formation of the Furutobe Kuroko ore deposit – and exploration at the Furutobe mine (II). Mining Geology, 27, 9-22 (in Japanese).

Lackschewitz, K.S., Devey, C.W., Stoffers, P., Botz, R., Eisenhauer, A., Kummetz, M., Schmidt, M., Singer, A., 2004. Mineralogical, geochemical and isotopic characteristics of hydrothermal alteration processes in the active, submarine, felsic-hosted PACMANUS field, Manus Basin, Papua New Guinea. Geochimica et. Cosmochimica Acta, 68, 4405-4427.

Large, R.R., Gemmell, J.B., Paulick H., 2011a. The Alteration Box Plot: a simple approach to understanding the relationship between alteration mineralogy and lithogeochemistry associated with volcanic-hosted massive sulfide deposits. Economic Geology, 96, 957-971.

Large, R.R., McPhie, J., Gemmell, J.B., Hermann, W., Davidson, G., 2001b. The spectrum of ore deposit types, volcanic environments, alteration halos, and related exploration vectors in submarine volcanic successions: some examples from Australia. Economic Geology, 96, 913-938.

Leat, P.T., Jackson, S.E., Thorpe, R.S., Stillman, C.J., 1986. Geochemistry of bimodal basalt-subalkaline/peralkaline rhyolite provinces within the Southern British Caledonides. Journal of the Geological Society, London, 143, 259-273.

Lee, C., Shor, G.G., Bibee, L.D., Lu, R.S., Hilde, T.W.C., 1980. Okinawa Trough, origin of a back-arc basin. Marine Geology, 35, 219–241.

Lentz, D.R., Hall, D.C., Hoy, L.D., 1997. Chemostratigraphic, alteration, and oxygen isotopic trends in a profile through the stratigraphic sequence hosting the Heath Steel B Zone massive sulfide deposit, New Brunswick. The Canadian Mineralogist, 35, 841-874.

Lesher, C.M., Goodwin, A.M., Campbell, I.H., Gorton, M.P., 1986. Trace-element geochemistry of ore-associated and barren, felsic metavolcanic rocks in the Superior Province, Canada. Canadian Journal of Earth Sciences, 23, 222-237.

Letouzey, J., Kimura, M., 1986. The Okinawa Trough: genesis of a back-arc basin developing along a continental margin. Tectonophysics, 125, 209–230.

Lüders, V., Pracejus, B., Halback, P., 2001. Fluid inclusion and sulfur isotope studies in probable modern analogue for Kuroko-type ores from the JADE hydrothermal field (Central Okinawa Trough, Japan). Chemical Geology, 173, 45-58.

MacLean, W.H., Barrett, T.J., 1993. Lithogeochemical techniques using immobile elements. Journal of Geochemical Exploration, 48, 109-133.

MacLean, W.H., Hoy, L.D., 1991. Geochemistry of hydrothermally altered rocks at the Horne Mine, Noranda, Quebec. Economic Geology, 86, 506-528.

MacLean, W.H., Kranidotis, P. 1987. Immobile elements as monitors of mass transfer in hydrothermal alteration: Phelps Dodge massive sulfide deposit, Matagami, Quebec. Economic Geology, 82, 951-962.

Masaki, Y., Kinoshita, M., Inagaki, F., Nakagawa, S., Takai, K., 2011. Possible kilometer-scale hydrothermal circulation within the Iheya-North field, mid-Okinawa Trough, as inferred from heat flow data. JAMSTEC Rep. Res. Dev. 12, 1-12Mayer J.W. (1977) Ion Beam Handbook for Material Analysis. Academic Press, New York

McConachy, T.F., Arculus, R.J., Yeats, C.J., Barriga, F.J.A.S., McInnes, B.I.A., Sestak, S., Sharpe, R., Rakau, B., Tevi, T., 2005. New hydrothermal activity and alkalic volcanism in the backarc Coriolis Troughs, Vanuatu. Geology, 33, 61-64.

McConnell, B.J., Stillman, C.J., Hertogen, J. 1991. An Ordovician basalt to peralkaline rhyolite fractionation series from Avoca, Ireland. Journal of the Geological Society, London, 148, 711-718.

McLeod, R.L., Stanton, R.L., 1984. Phyllosilicates and associated minerals in some Paleozoic stratiform sulfide deposits of Southeastern Australia. Economic Geology, 79, 1-22.

Mottl, M.J., Wheat, C.G., Boulègue, J., 1994. Timing of ore deposition and sill intrusion at Site 856: evidence from stratigraphy, alteration, and sediment pore-water composition, in Mottl, M.J., Davis, E.E., Fisher, A.T. & Slack, J.F. (Eds.), Proc. ODP, Sci. Results, 139: College Station, TX (Ocean Drilling Program), 679–693. doi:10.2973/odp.proc.sr.139.232.1994

Nakagawa, S., Takai, K., Inagaki, F., Chiba, H., Ishibashi, J., Kataoka, S., Hirayama, H., Nunoura, T., Horikoshi, K., Sako, Y., 2005. Variability in microbial community and venting chemistry in a sediment-hosted backarc hydrothermal system: impacts of subseafloor phase-separation. FEMS Microbiol. Ecol. 54, 141-155.

Oiwane, H., Kumagai, H., Masaki, Y., Tokuyama, H., Kinoshita, M., 2008. Characteristics of sediment in Iheya North Knoll and the ‘acoustic blanking layer’. Japanese Geoscience Union Meeting. J164-013.

Paulick, H., Bach, W., 2006. Phyllosilicate alteration mineral assemblages in the active subsea-floor Pacmanus hydrothermal system, Papua New Guinea, ODP Leg 193. Economic Geology, 101, 633-650.

Paulick, H., Herrmann, W., Gemmell, J.B., 2001. Alteration of felsic volcanics hosting the Thalanga massive sulfide deposit (Northern Queensland, Australia) and geochemical proximity indicators to ore. Economic Geology, 96, 1175-1200.

Pearce, J.A., 1996. A user's guide to basalt discrimination diagrams, in: Wyman, D.A. (Ed.), Trace element geochemistry of volcanic rocks: applications for massive sulphide exploration. Geological Association of Canada, pp. 79-113.

Pearce, J.A., Harris, N.B.W., Tindle, A.G., 1984. Trace element discrimination diagrams for the tectonic interpretation of granitic rocks. Journal of Petrology, 25, 956-983.

Petersen, S., Monecke, T., Westhues, A., Hannington, M.D., Gemmell, J.B., Sharpe, R., Peters, M., Strauss, H., Lackschewitz, K., Augustin, N., Gibson, H., Kleeberg, R., 2014. Drilling shallow-water massive sulfides at the Palinuro Volcanic Complex, Aeolian Island Arc, Italy. Economic Geology, 109, 2129-2157.

Piercey, S.J., 2007. Volcanogenic massive sulphide (VMS) deposits of the Newfoundland Appalachians: an overview of their setting, classification, grade-tonnage data, and unresolved questions, in: Pereira, C.G.P., Walsh, D.G. (Eds.), Current Research. Newfoundland Department of Natural Resources, Geological Survey, Report 07-01, 169-178.

Piercey, S.J., 2009. Lithogeochemistry of volcanic rocks associated with volcanogenic massive sulphide deposits and applications to exploration. In: Cousens, B., Piercey, S.J. (eds). Submarine volcanism and mineralization: modern through ancient. Geological Association of Canada, Short Course 29-30 May 2008, Canada, p15-40.

Piercey, S.J., 2011. The setting, style, and role of magmatism in the formation of volcanogenic massive sulphide deposits. Mineralium Deposita, 46, 449-471.

Prior, D.J., Mariani, E., Wheeler, J., 2009. EBSD in the earth sciences: applications, common practice and challenges, in: Schwartz, A.J., Kumar, M., Adams, B. L., Field, D.P. (Eds.), Electron Backscatter Diffraction in Materials Science. Springer Berlin, pp. 345-360.

Prior, D.J., Boyle, A.P., Brenker, F., Cheadle, M.C., Day, A., Lopez, G., Peruzzo, L., Potts, G.J., Reddy, S., Spiess, R., Timms, N.E., Trimby, P., Wheeler, J., Zetterstrom, L., 1999. The application of electron backscatter diffraction and orientation contrast imaging in the SEM to textural problems in rocks. American Mineralogist, 84, 1741-1759.

Roberts, S., Bach, W., Binns, R.A., Vanko, D.A., Yeats, C.J., Teagle, D.A.H., Blacklock, K., Blusztajn, J.S., Boyce, A.J., Cooper, M.J., Holland, N., McDonald, B., 2003. Contrasting evolution of hydrothermal fluids in the PACMANUS system, Manus Basin: the Sr and S isotope evidence. Geology, 31, 805-808.

Sánchez-España, J., Velasco, F., Yusta, I., 2000. Hydrothermal alteration of felsic volcanic rocks associated with massive sulphide deposition in the northern Iberian Pyrite Belt (SW Spain). Applied Geochemistry, 15, 1265-1290.

Sato, T., 1974. Distribution and geological setting of the Kuroko deposits. In: Ishihara, S (ed.) Geology of Kuroko deposits. Mining Geology Special Issue 6, 1-10.

Sato, T., 1977. Kuroko deposits: their geology, geochemistry and origin. Geological Society, London, Special Publications, 7, 153-161.

Schmidt, J.M., 1988. Mineral and whole-rock compositions of seawater-dominated hydrothermal alteration at the Arctic volcanogenic massive sulfide prospect, Alaska. Economic Geology, 83, 822-842.

Shanks III, W.C., 2012. Hydrothermal alteration in volcanogenic massive sulfide occurrence model. U.S. Geological Survey Scientific Investigations Report 2010-5070, Chapter 11, 12p.

Shao, H., Yang, S., Wang, Q., Guo, Y., 2015. Discriminating hydrothermal and terrigenous clays in the Okinawa Trough, East China Sea: evidences from mineralogy and geochemistry. Chemical Geology. Doi:10.1016/j.chemgeo.2015.02.001

Shikazono, N., Holland, H.D., Quirk, R.D., 1983. Anhydrite in Kuroko deposits: mode of occurrence and depositional mechanisms. In: Ohmoto, H., Skinner, B.J. (eds.) Kuroko and related volcanogenic massive sulfide deposits. Economic Geology, Monograph 5, 329-344.

Shinjo, R., Chung, S.-l., Kato, Y., Kimura, M., 1999. Geochemical and Sr-Nd isotopic characteristics of volcanic rocks from the Okinawa Trough and Ryukyu Arc: implications for the evolution of a young, intracontinental back arc basin. Journal of Geophysical Research, 104, 10591-10608.

Shinjo, R., Kato, Y., 2000. Geochemical constraints on the origin of bimodal magmatism at the Okinawa Trough, an incipient back-arc basin. Lithos, 54, 117-137.

Shinjo, R., Woodhead, J.D., Hergt, J.M., 2000. Geochemical variation within the northern Ryukyu Arc: magma source compositions and geodynamic implications. Contributions to Mineralogy and Petrology, 140, 263-282.

Sibuet, J.-C., Deffontaines, B., Hsu, S.-K., Thareau, N., Le Formal, J.-P., Liu, C.-S., ACT party., 1998. Okinawa Trough backarc basin: early tectonic and magmatic evolution. Journal of Geophysical Research, 103, 30245-30267.

Sibuet, J.-C., Letouzey, J., Barbier, F., Charvet, J., Foucher, J.P., Hilde, T.W.C., Kimura, M., Chiao, L.Y., Marsset, B., Muller, C., Stephan, J.F., 1987. Back arc extension in the Okinawa Trough. Journal of Geophysical Research, 92, 14041-14063.

Sturz, A. Itoh, M., Smith, S., 1998. Mineralogy and geochemical composition of clay minerals, TAG hydrothermal mound, in: Herzig, P.M., Humphris, S.E., Miller, D.J. & Zierenberg, R.A. (Eds.). Proceedings of the Ocean Drilling Program, Scientific Results, 158, 277-284.

McDonough, W.F., Sun, S-S., 1995. The composition of the Earth. Chemical Geology, 120, 223–254.

Takai, K., Mottl, M.J., Nielsen, S.H.H., the Expedition 331 Scientists, 2011. Proceedings of IODP 331. Tokyo (Integrated Ocean Drilling Program Management International, Inc). Doi:10.2204/iodp.proc.331.2011.

Takai, K., Mottl, M.J., Nielsen, S.H.H., the Expedition 331 Scientists, 2012. IODP Expedition 331: strong and expansive subseafloor hydrothermal activities in the Okinawa Trough. Scientific Drilling, 13, 19-27. DOI: 10.2204/iodp.sd.13.03.2011.

Teagle, D.A.H., Alt, J.C., Chiba, H., Humphris, S.E., Haliday, A.N., 1998. Strontium and oxygen isotopic constraints on fluid mixing, alteration and mineralization in the TAG hydrothermal deposit. Chemical Geology, 149, 1-24.

Tindle, A. 2015. Chlorite mineral calculation worksheet. Available at: http://www.open.ac.uk/earth-research/tindle/AGTWebPages/AGTSoft.html

Trimby, P.W., Prior, D.J., Wheeler, J., 1998. Grain boundary hierarchy development in a quartz mylonite. Journal of Structural Geology, 20, 917-935.

Tsuji, T., Takai, K., Oiwane, H., Nakamura, Y., Masaki, Y., Kumagai, H., Kinoshita, M., Yamamoto, F., Okana, T., Kuramoto, S., 2012. Hydrothermal fluid flow system around the Iheya North Knoll in the mid-Okinawa trough based on seismic reflection data. Journal of Volcanology and Geothermal Research, 213-214, 41-50.

Ueno, H., Hamasaki, H., Murakawa, Y., Kitazono, S., Takeda, T., 2003. Ore and gangue minerals of sulfide chimneys from the North Knoll Iheya Ridge, Okinawa Trough, Japan. JAMSTEC Journal of Deep Sea Research, 22, 49-62.

van Staal, C.R., 2007. Pre-Carboniferous tectonic evolution and metallogeny of the Canadian Appalachians, in: Goodfellow, W.D. (Ed.), Mineral Deposits of Canada: a synthesis of major deposit types, district metallogeny, the evolution of geological provinces, and exploration methods. Geological Association of Canada, Mineral Deposits Division, Special Publication No. 5, pp793-818.

Webber, A.P., Roberts, S., Burgess, R., Boyce, A.J., 2011. Fluid mixing and thermal regimes beneath the PACMANUS hydrothermal field, Papua New Guinea: helium and oxygen isotope data. Earth and Planetary Science Letters, 304, 93-102.

Webber, A.P., Roberts, S., Murton, B.J., Hodgkinson, M.R.S., 2015. Geology, sulphide geochemistry and supercritical venting at the Bebe hydrothermal vent field, Cayman Trough. Geochemistry, Geophysics, Geosystems. Online First. DOI: 10.1002/2015GC005879.

Yamada, R., Yoshida, T., 2011. Relationships between Kuroko volcanogenic massive sulfide (VMS) deposits, felsic volcanism, and island arc development in the northeast Honshu arc, Japan. Mineralium Deposita, 46, 431-448.

Yamano, M., Uyeda, S., Kinoshita, H., Hilde, T.W.C., 1986. Report on DEL1984 cruises in the middle Okinawa Trough. 4. Heat flow measurements. Bull. Earthquake Res. Int. Univ. Tokyo, 61, 251-267.

Yeats, C., 2012. Deep sea mining: exploration is inevitable. http://www.scidev.net/global/earth-science/opinion/deep-sea-mining-exploration-is-inevitable.html

Yeats, C.J., Parr, J.M., Binns, R.A., Gemmell, J.B., Scott, S.D., 2014. The Susu Knolls hydrothermal field, Eastern Manus Basin, Papua New Guinea: an active submarine high-sulfidation copper-gold system. Economic Geology, 109, 2207-2226.

Zhang, W., Fyfe, W.S., 1995. Chloritization of the hydrothermally altered bedrock at the Igarapé Bahia gold deposit, Carajás, Brazil. Mineralium Deposita, 30, 30-38.

Zeng, Z.G., Jiang, F.Q., Zhai, S.K., Qin, Y.S., 2000. Lead isotopic compositions of massive sulfides from the Jade hydrothermal field in the Okinawa Trough and its geological significance. Geochimica, 29, 239-245 (in Chinese with English Abstract).

Zeng, Z., Yu, S., Wang, X., Fu, Y., Yin, X., Zhang, G., Wang, X., Chen, S., 2010. Geochemical and isotopic characteristics of volcanic rocks from the northern East China Sea shelf margin and the Okinawa Trough. Acta Oceanologica Sinica, 29, 48-61.

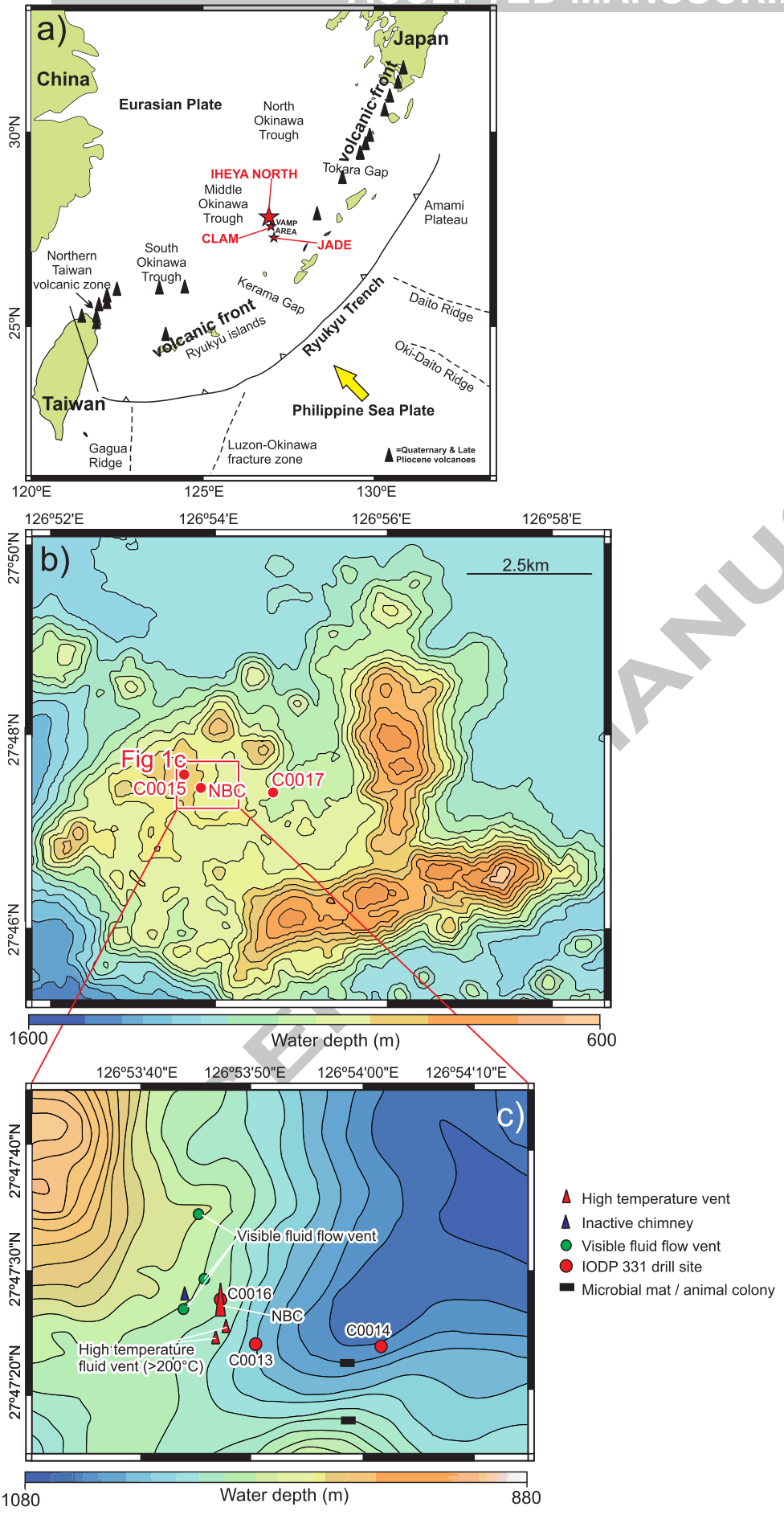

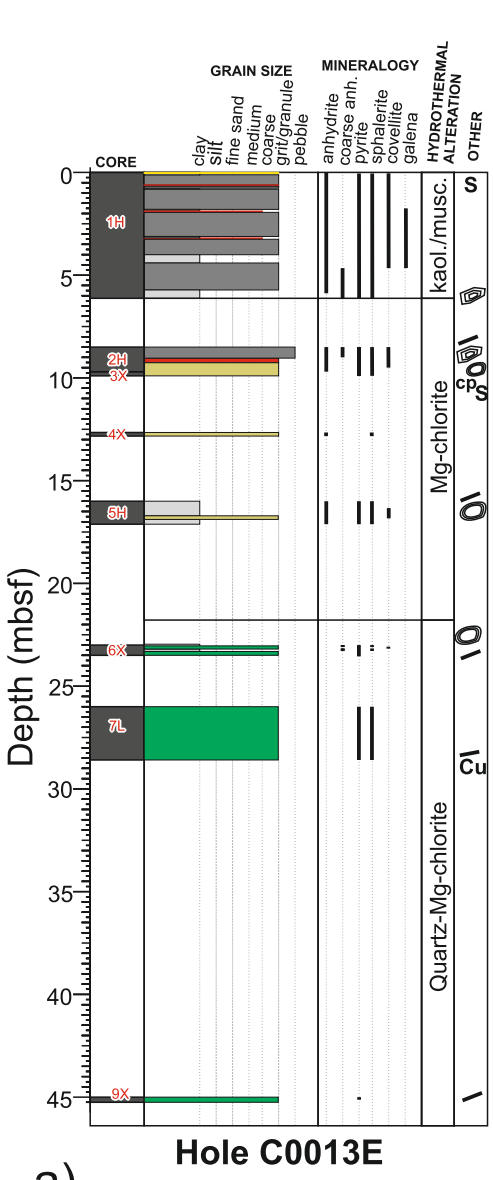

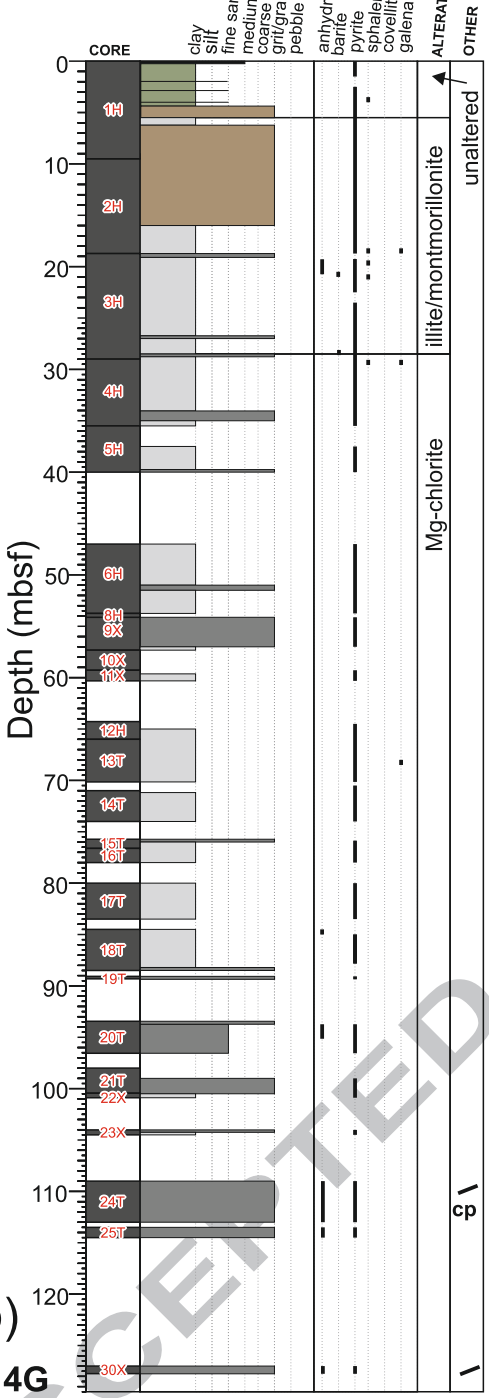

Legend

Medium- to coarse-grained sulfidic sediment. Sulfides dominated by pyrite-sphalerite with minor galena and covellite. Some coarse (1-4 cm) fragments of cemented sulfide aggregates.

Reduced mud (unaltered). Dark olive green colour, with foraminifera and very fine disseminated pyrite.

Hydrothermal clay. Light to medium grey colour. May contain pseudoclasts of harder clay after pumice(?).

Unaltered/weakly-altered pumiceous grit/gravel. Pumice clasts in a coarse sand matrix with dark olive green mud. Often clast supported.

Hydrothermal grit/gravel. Scattered large (1-2cm) aggregate clasts set in a clay-sand matrix. Locally sulfide rich (to ~5%). Grey to black colour, occasionally paler. Can be clast- or matrix-supported. Pumice replaced by white to pale grey clay.

Hydrothermal grit with native sulfur. Pale grey to yellow colour. Patches of white clay. Small aggregates of altered volcanic rocks.

Anhydrite-carbonate-silica vein material embedded in dark and white clay.

White to pale grey volcanic breccia.
Strongly altered volcanic rock comprising clasts in a silicified network of quartz veins (hairline to 1cm in width).
Clasts are <0.5cm to >5cm, poorly-sorted, subangular to subrounded, and in some areas jig-saw fit.

Sulfide vein.

Broken anhydrite crystals (to 5mm in size) - veins disturbed by drilling?

S Native sulfur stringers and/or blebs.

Large (4-5cm), white, hard, anhydrite-clay-sulfide nodules (grown *in situ*?). May also contain dolomite, calcite, quartz and/or talc.

cp Presence of trace chalcopyrite.

Cu Presence of native copper in basement.

Note: Sections of re-drilled core not shown.

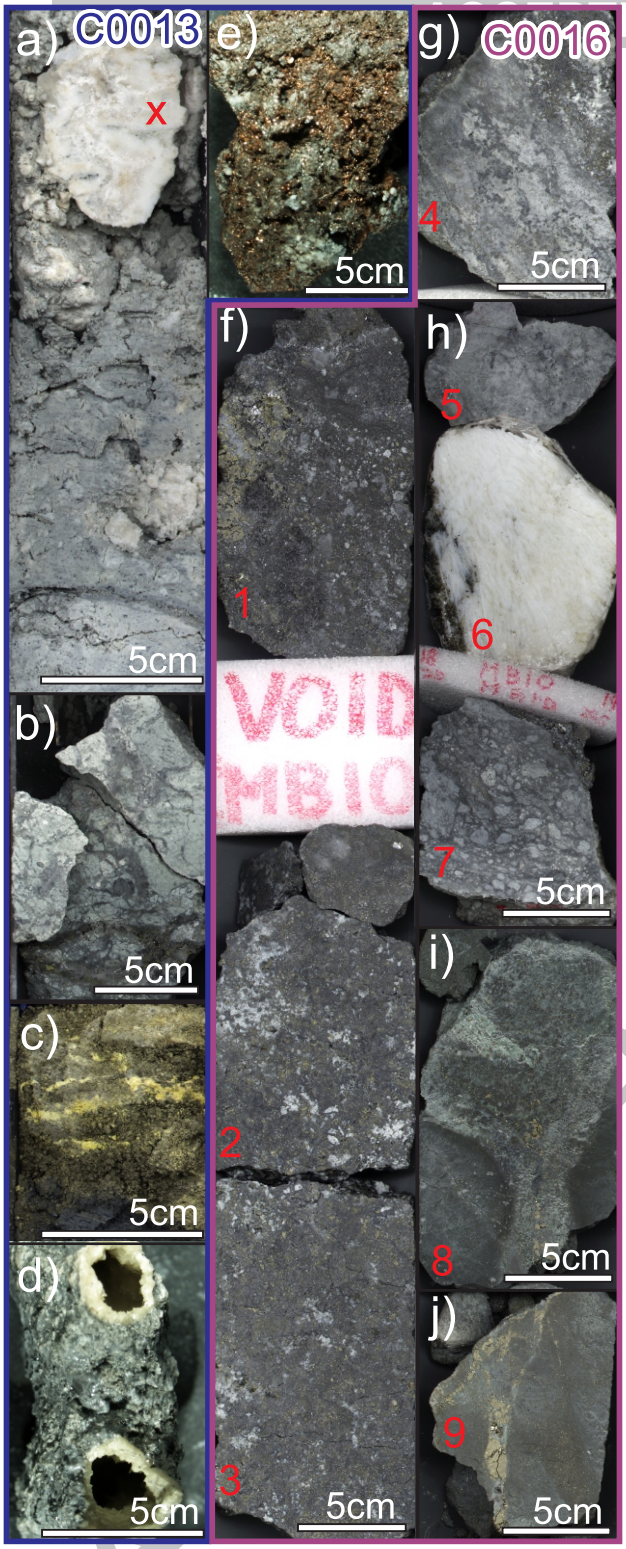

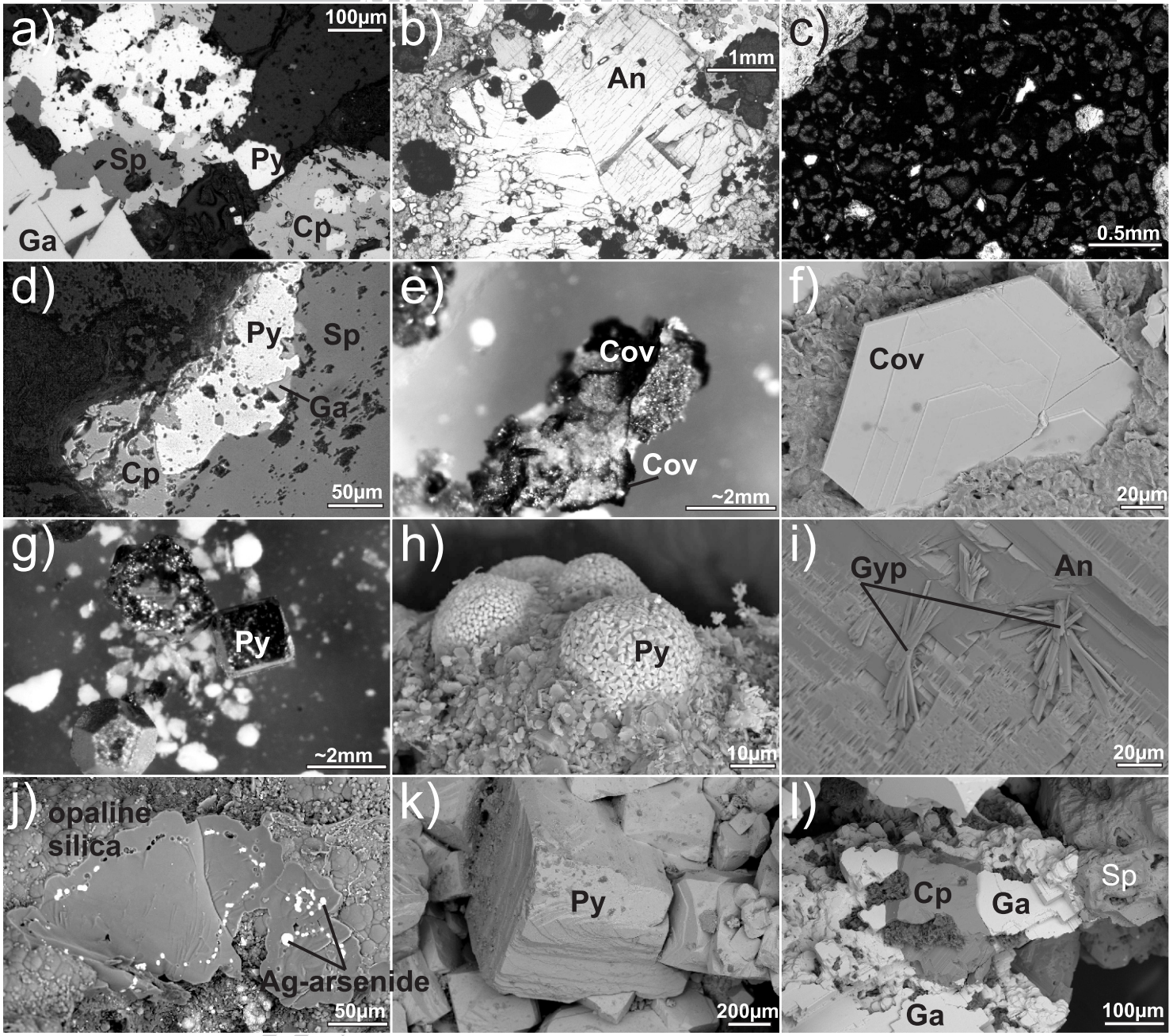

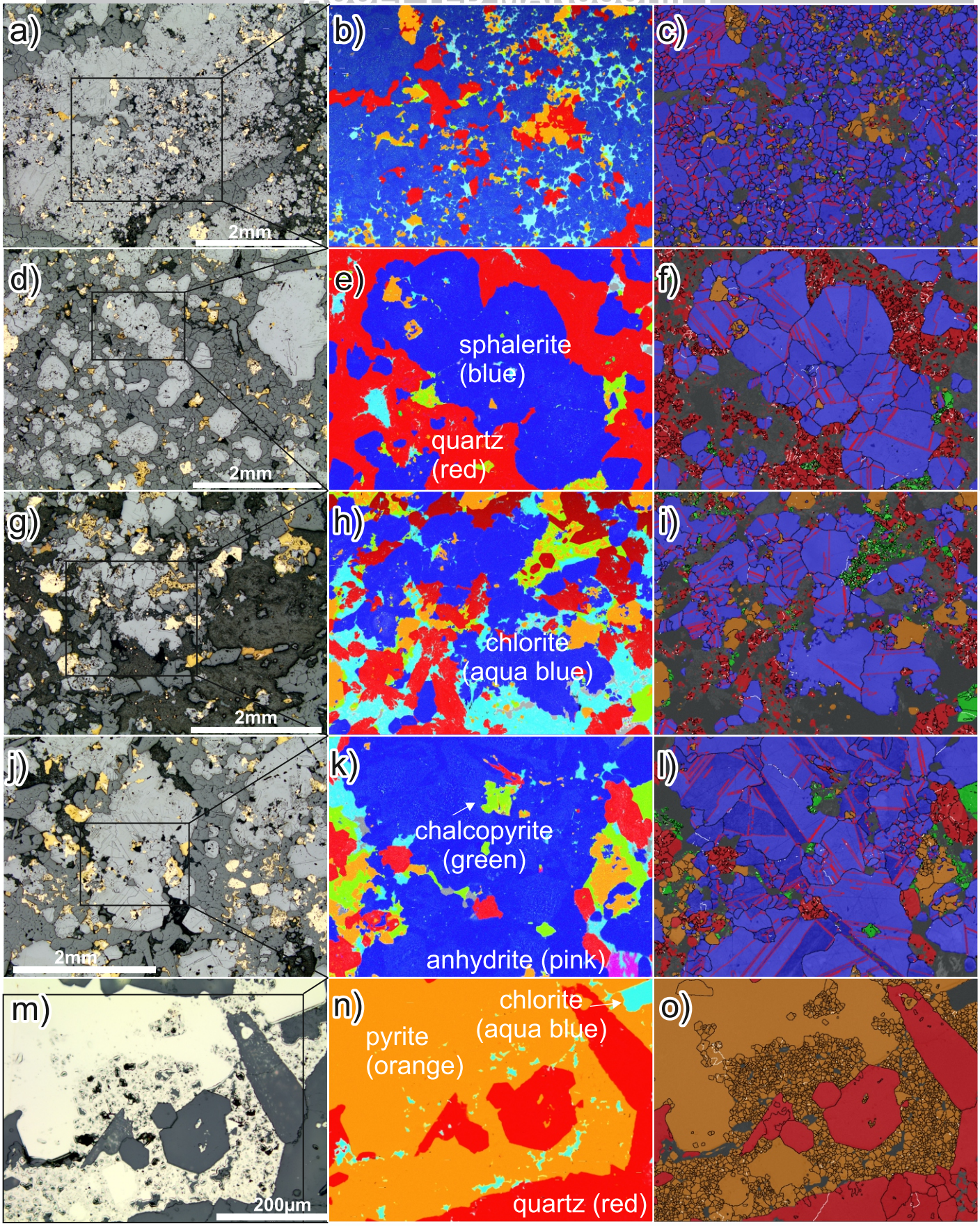

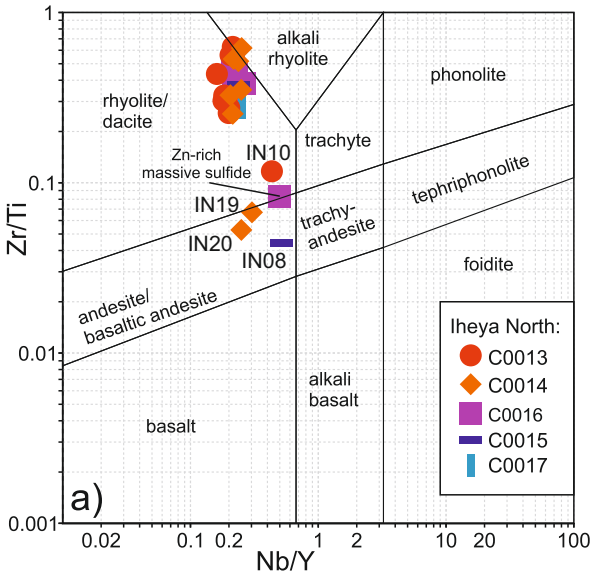

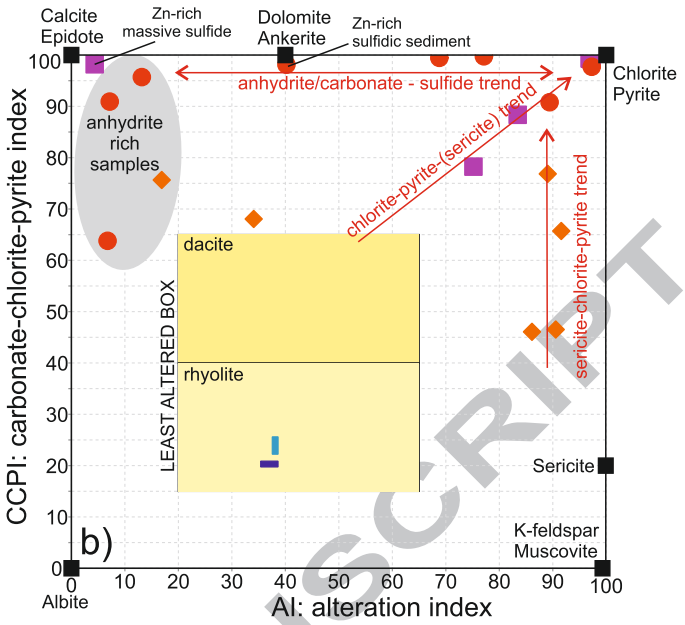

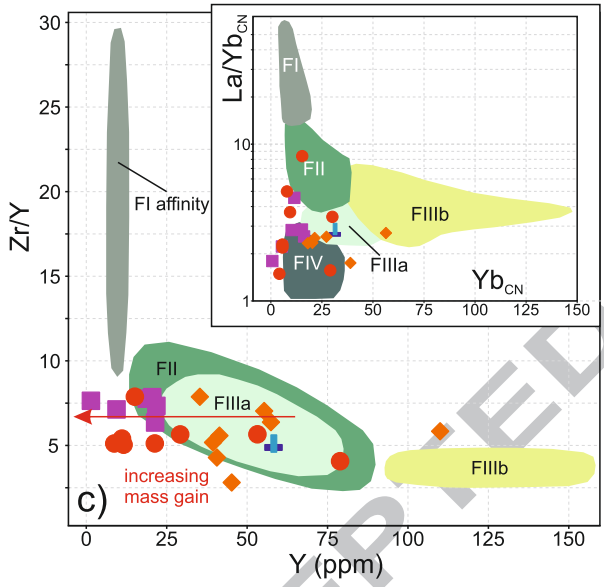

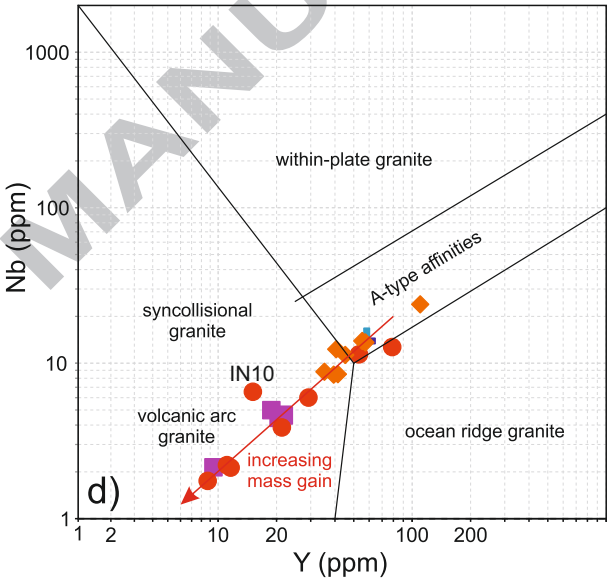

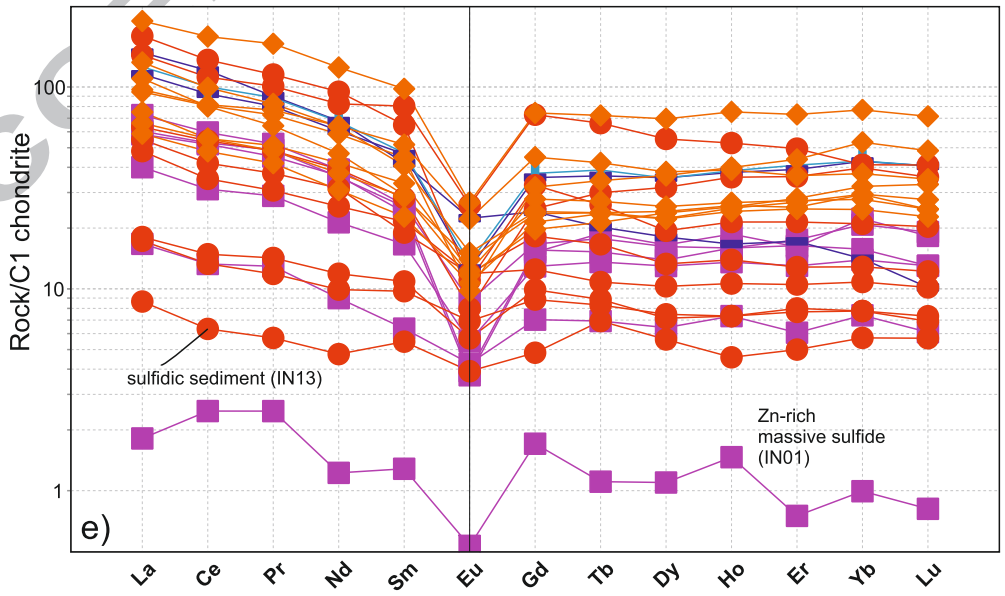

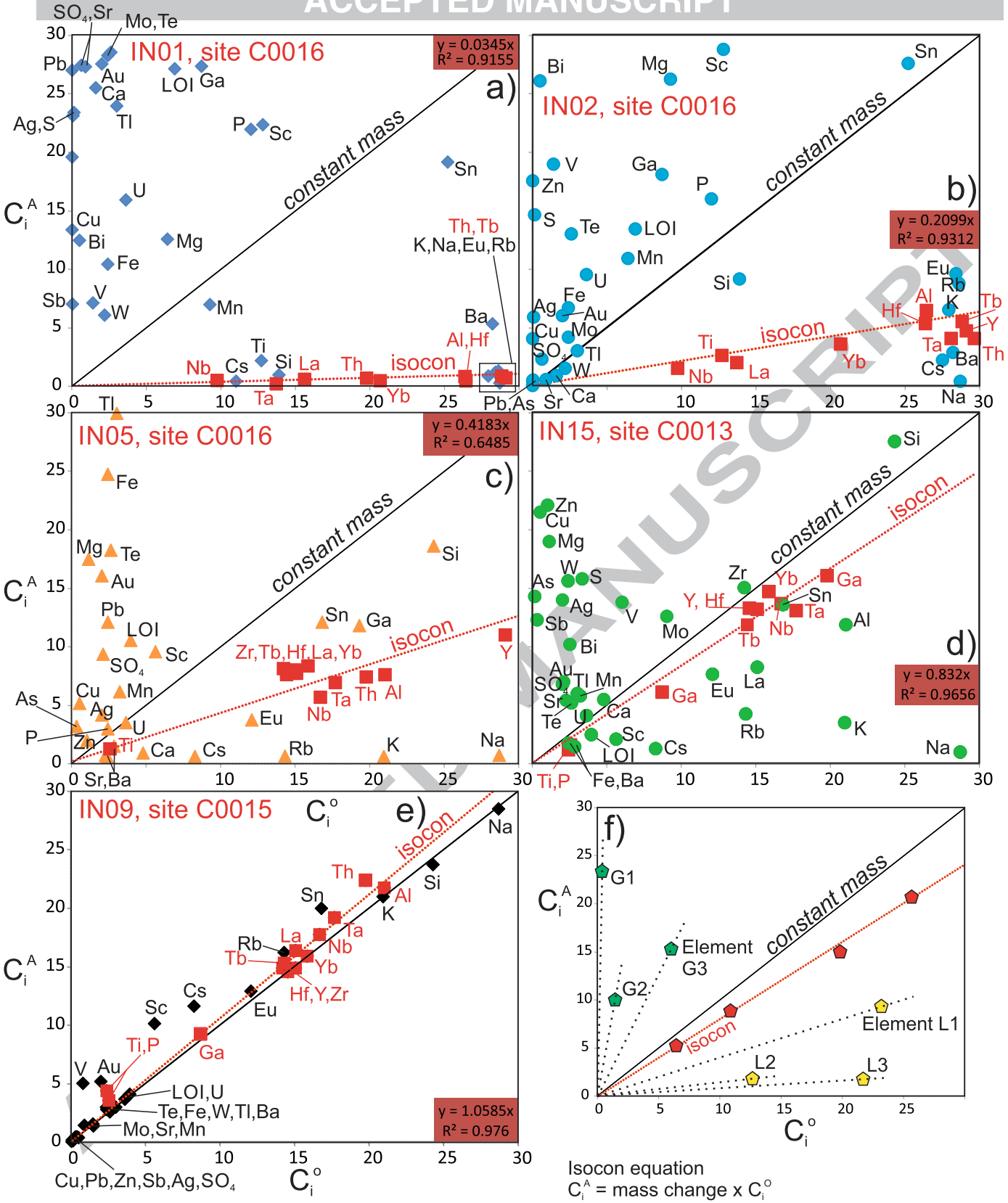

Immobile element used for isocon

Mobile element - removed from rock (below isocon)

Mobile element - added to rock (above isocon)

Isocon equation

C_i^A = mass change x C_i^o

Relative magnitude of mass gains/losses for mobile elements:
G1>G2>G3 (i.e. steeper slope from origin of graph)
L3>L2>L1 (i.e. shallower slope from origin of graph)

Note: The isocon plots below the line of constant mass, therefore the rock has gained mass.

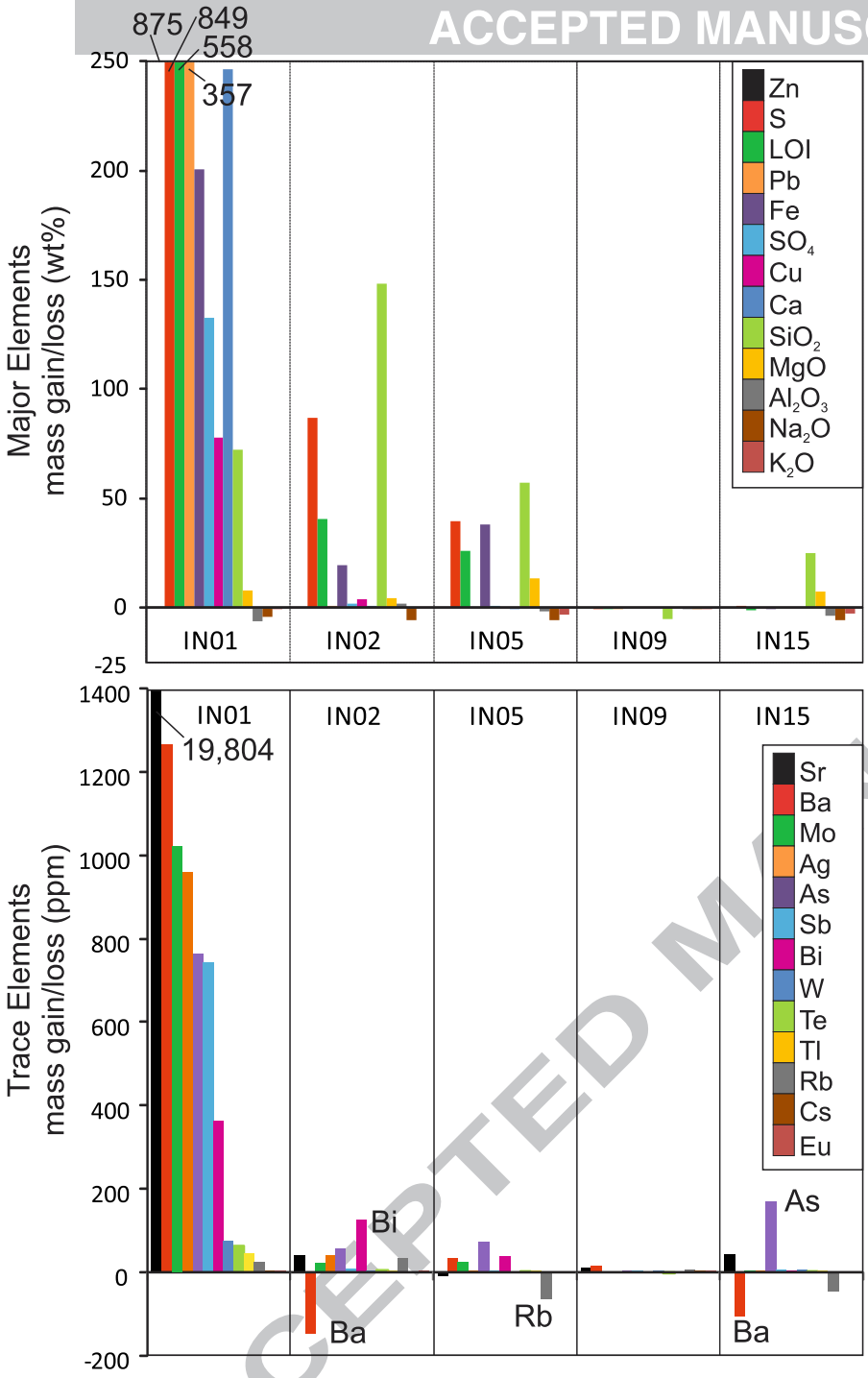

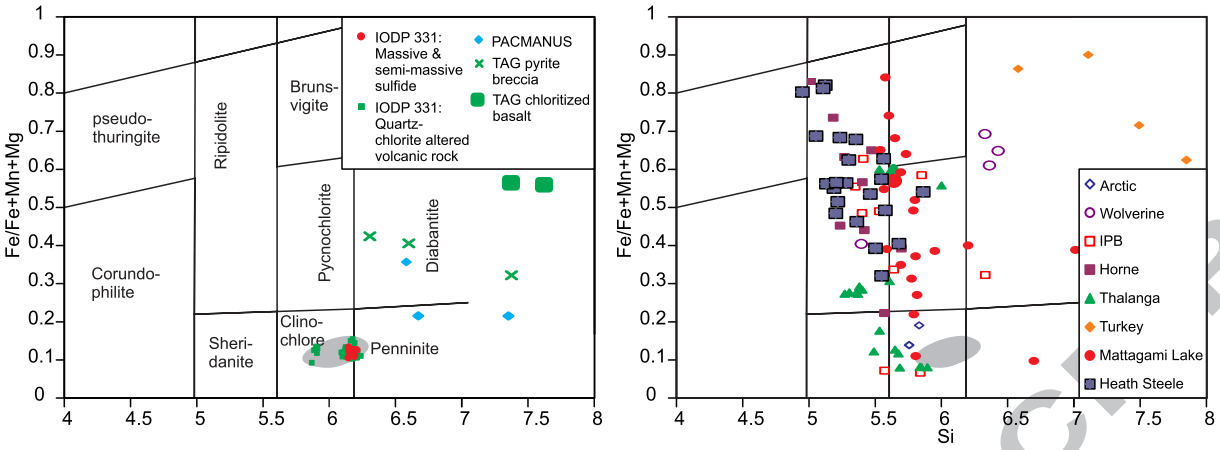

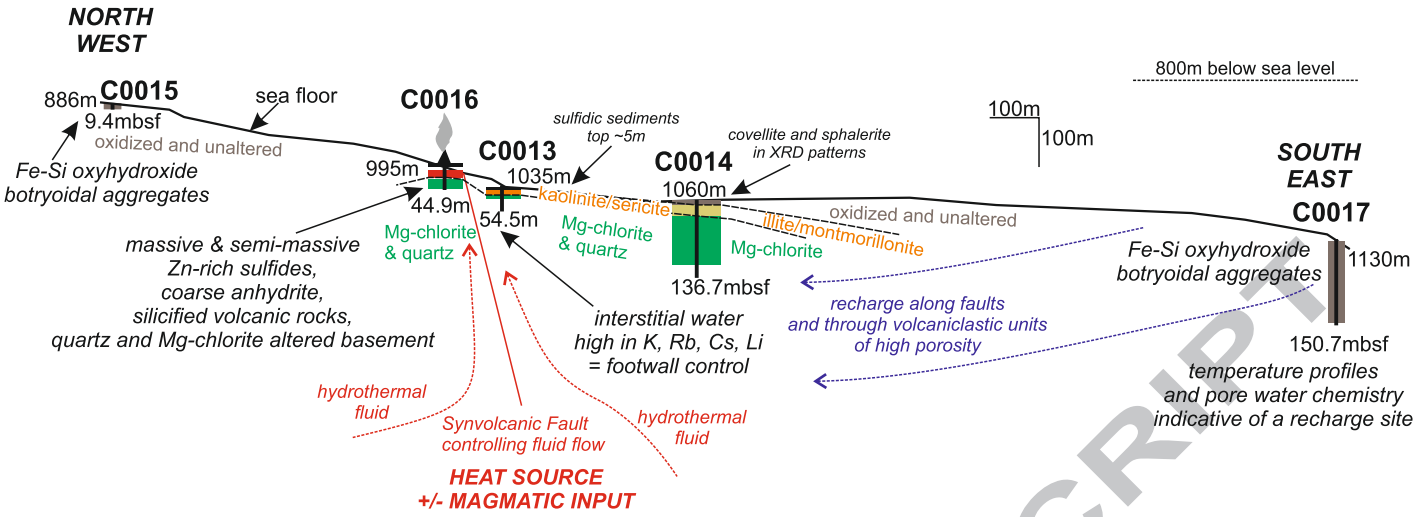

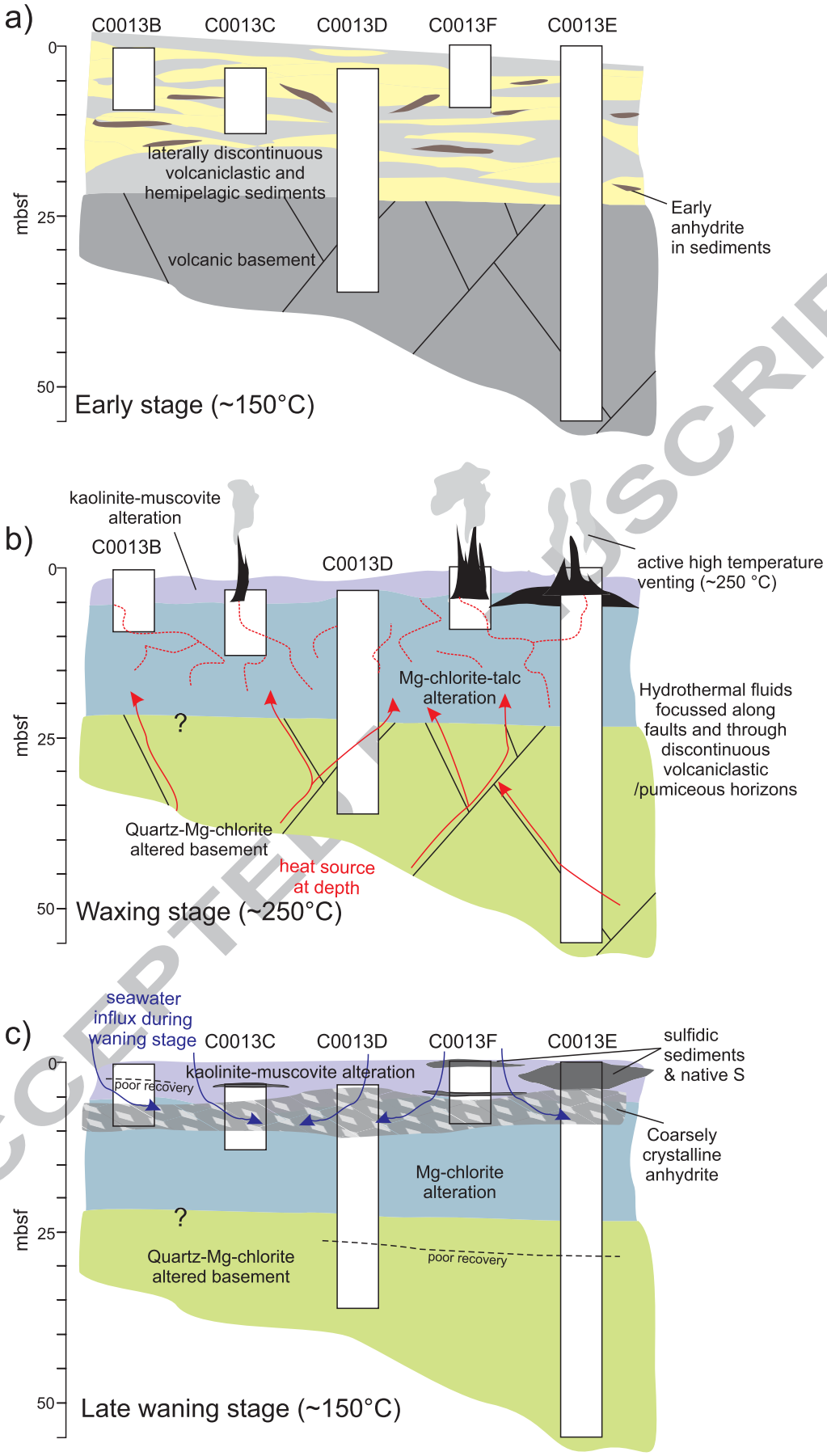

Table 1. Whole rock geochemical data from Iheya North.

	Units	IN01	IN02	IN03	IN04	IN05	IN06	IN07	IN08	IN09	IN10	IN11	IN12	IN13
Site	C00	16	16	16	16	16	16	17	17	15	13	13	13	13
Hole		B	B	B	B	B	B	C	D	B	C	C	D	E
Core		1	1	2	2	3	3	2	9	1	1	1	1	1
Section		1	cc	cc	cc	1	cc	5	4	2	4	16	6	4
From	cm	11	12	0	21	31	12	17	95	8	75	25	57	22
To	cm	14	14	3	26	34	14	19	97	10	77	27	59	24
Depth at site	m	0.1	0.8	9.0	9.2	27.3	27.7	32.7	125.4	1.46	5.5	12.0	9.6	2.2
Lithology		Sphalerite-rich massive sulfide (clastic-texture)	Silicified felsic volcanic rock with vein and disseminated sulfides	Silicified felsic volcanic rock with disseminated pyrite	Silicified felsic volcanic rock with disseminated pyrite	Silicified-chloritized felsic volcanic rock w. sulfide veining	Silicified-chloritized felsic volcanic rock w. sulfide veining	Grey woody pumice	Brown hemipelagic clay	Pumice (with trace yellow weakly oxidized clay)	Dark grey clay-altered (kaolinite/muscovite) pumiceous volcaniclastic with anhydrite and sulfides	Pale grey clay-altered (Mg-chlorite) pumiceous volcaniclastic with anhydrite	Clay-altered (Mg-chlorite) pumiceous volcaniclastic with quartz-carbonate clast	Black sulfidic unconsolidated sediment (grit)
SiO_2	%	4.89	45.71	79.45	80.44	53.05	55.93	69.40	60.52	67.82	11.82	10.49	4.76	0.87
TiO_2		0.02	0.03	0.06	0.06	0.05	0.06	0.13	0.70	0.18	0.17	0.04	0.03	0.03
Al_2O_3		0.21	2.93	4.16	4.50	4.27	3.94	12.01	14.13	12.43	6.62	1.89	1.71	0.17
Fe		6.97	4.45	3.73	3.06	16.50	15.66	1.60	3.70	1.87	1.18	0.34	0.49	6.74
MnO		0.13	0.11	0.04	0.04	0.12	0.11	0.06	0.07	0.07	0.01	0.07	1.22	0.30
MgO		0.28	1.05	0.99	1.03	5.81	5.22	0.37	2.62	0.58	1.02	4.86	32.60	0.42
CaO		8.52	0.29	1.68	0.69	0.08	0.03	0.53	4.10	0.63	28.76	32.25	9.61	0.61
K_2O		0.11	0.81	1.21	1.30	0.07	0.10	3.49	3.14	3.50	1.09	0.06	0.02	0.06
Na_2O		0.06	0.08	0.10	0.08	0.11	0.12	6.04	1.86	6.00	0.35	0.18	0.07	0.11
P		0.011	0.008	0.004	0.003	0.007	0.007	0.006	0.066	0.011	0.009	0.006	0.007	0.012
Zn		30.20	27.00	0.62	2.01	0.02	0.02	0.01	0.01	0.03	0.28	0.06	0.38	43.20
Pb		12.30	0.20	0.03	0.05	0.02	0.01	0.00	0.01	0.00	0.28	0.00	0.18	4.39
Cu		2.68	0.81	0.02	0.15	0.01	0.01	<0.001	0.00	0.00	0.10	0.01	0.01	5.36
BaO		0.02	0.01	<0.01	<0.01	0.03	0.03	0.03	0.05	0.04	0.30	0.02	0.01	0.01
S		29.30	18.30	5.15	4.21	16.60	15.90	0.17	0.48	0.17	17.90	18.70	5.91	33.60
LOI		19.42	9.59	4.19	3.60	13.04	11.97	4.92	5.97	5.14	5.52	3.00	34.29	21.08
Sulfate		4.58	0.38	0.98	0.46	0.46	0.46	0.10	0.23	0.14	16.30	18.00	4.87	1.36
C		0.06	0.05	0.06	0.06	0.05	0.05	0.06	1.11	0.07	0.08	0.06	9.18	0.12
Ag	ppm	33.1	8.4	2.4	3.3	0.2	0.3	<0.1	0.3	<0.1	26.4	<0.1	0.7	42.2
As		26.4	12.0	35.0	10.6	30.6	24.4	1.4	9.6	5.6	183	0.6	10.2	15000
Ba		53.5	28.5	27.5	64.5	131	148	282	442	312	2480	5.5	17	67.5
Be		<0.2	<0.2	0.6	1.8	1.0	0.4	2.8	3.2	3.0	0.6	0.6	0.6	<0.2
Bi		12.5	26.1	5.68	12.3	15.9	15.7	0.5	0.34	0.4	1.14	0.04	0.16	14.3
Cd		738.0	663.0	20.7	65.9	0.8	0.3	0.5	0.3	1.1	8.4	1.4	11.8	980
Ce		1.52	8.14	36.5	19.1	31.9	32.4	56.7	74	61.5	25.7	9.1	8.16	3.88
Cs		0.11	0.22	0.48	0.66	0.14	0.12	2.75	9.11	3.88	2.6	0.26	0.14	0.14
Dy		0.27	1.58	3.98	3.19	4.06	3.42	8.74	4.44	8.7	2.53	1.76	1.84	1.38
Er		0.12	0.97	2.62	2.08	2.58	2.8	6.25	2.75	6.56	1.68	1.28	1.23	0.8
Eu		0.03	0.24	0.49	0.31	0.21	0.22	0.71	1.26	0.76	0.67	0.32	0.39	0.22
Ga		60.9	40.2	9.3	11	11.7	10.2	19.3	16.4	20.5	9.8	3.4	4	49.4
Gd		0.34	1.4	3.32	2.57	3.02	3.1	7.08	4.79	7.43	2.48	1.97	1.76	0.96
Ge		9.3	3.25	1.15	1.05	1.75	1.7	1.45	3.25	1.75	0.85	0.25	0.2	256
Hf		0.24	1.52	3.05	3.32	3.94	3.6	7.53	4.5	7.45	3.48	1.31	1.19	0.88
Ho		0.08	0.4	0.87	0.74	1.02	0.87	2.06	0.91	2.1	0.58	0.4	0.4	0.25

La		0.43	3.96	17.2	9.49	13.8	14.3	27.4	35.1	29.8	13	4.28	4.1	2.05
Lu		0.02	0.15	0.32	0.32	0.45	0.47	1.00	0.25	1.00	0.25	0.17	0.18	0.14
Mo		35.4	5.2	14.4	17.4	11	11.2	3.0	1.0	2.8	46.2	2.8	4.4	59
Nb		0.72	2.14	4.66	4.99	4.61	4.45	13.9	13.4	14.8	6.55	2.21	2.13	1.75
Nd		0.56	4.11	17.8	9.76	16.6	16.4	27.7	31	30.8	14.4	5.43	4.53	2.17
Pr		0.23	1.2	4.85	2.68	4.2	4.52	7.45	8.35	8.22	3.47	1.32	1.1	0.53
Rb		3.3	21.9	41	42.6	2.25	2.65	71.5	125	81.1	46.1	2.2	0.7	1.8
Re		0.07	<0.01	0.02	0.03	<0.01	<0.01	0.02	<0.01	<0.01	0.04	<0.01	0.01	0.04
Sb		25.6	1.8	4.5	9.4	1	0.8	0.1	2.7	1.0	351	7.8	2.5	104
Sc		2.8	3.6	2.4	1.1	2.7	2.2	1.6	13.3	2.9	2.9	1.1	1.3	2.9
Sm		0.19	0.94	3.85	2.46	3.54	3.77	6.89	6.2	6.97	2.81	1.61	1.44	0.81
Sn		3.2	4.6	3.0	3.2	3.0	3.0	4.2	5.4	5.0	2.6	1.0	1.2	2.0
Sr		684	13.4	99.1	36	5.0	2.8	22.4	195	36.3	1460	1240	472	55.3
Ta		0.04	0.15	0.32	0.37	0.4	0.4	1.04	0.99	1.13	0.61	0.16	0.16	0.11
Tb		0.04	0.25	0.64	0.49	0.68	0.55	1.31	0.73	1.4	0.39	0.32	0.3	0.25
Te		2.2	1.0	0.6	0.6	1.4	1.6	0.2	1.0	<0.2	<0.2	<0.2	<0.2	0.4
Th		0.35	1.35	3.16	3.5	3.64	3.5	9.88	12.8	11.2	6.39	1.32	1.45	0.92
Tl		1.6	<0.2	0.6	0.4	2.0	1.6	<0.2	<0.2	<0.2	0.8	<0.2	<0.2	<0.2
Tm		<0.01	0.12	0.38	0.77	0.44	0.43	1.14	0.39	1.03	0.25	0.18	0.18	0.12
U		11.4	6.8	20.4	13	2.38	2.08	2.58	2.53	2.63	16.2	0.63	1.43	2.5
V		10.2	27.1	43.6	31.8	15.7	13.3	2.0	94.9	12.6	23.3	0.7	1.5	4.7
W		2.65	0.65	0.45	2.5	0.15	0.25	0.95	1.75	1.20	2.95	0.20	1.20	11.60
Y		1.44	9.4	21.4	18.8	21.8	20.5	58.2	25.8	58.3	15.1	11.1	11.6	8.7
Yb		0.16	1.19	2.53	2.24	3.58	3.35	6.89	2.27	6.92	1.74	1.25	1.25	0.92
Zr		11	67	136	146	160	161	284	187	298	119	60	58.5	44.5
Au	ppb	69	15	42	22	40	31	5	3	13	39	3	5	17
Pt		1	1	<1	<1	<1	<1	1	<1	3	1	<1	<1	1
Pd		4	4	3	3	2	2	5	3	15	4	11	4	3

Table 1. (continued)

	Units	IN14	IN15	IN16	IN17	IN18	IN19	IN20	IN21	IN22	IN23	IN24	IN25
Site		13	13	13	14	13	14	14	14	14	14	14	14
Hole		E	E	E	G	F	G	G	G	G	G	G	G
Core		5	7	7	30	1	3	3	5	9	18	18	21
Section		1	2	2	1	cc	1	8	1	2	3	CC	3
From	cm	38	14	90	34	48	14	47	22	87	90	27	83
To	cm	40	16	96	36	50	16	49	23	89	92	29	84
Depth at site	m	16.4	26.5	27.2	127.5	8.7	18.8	25.7	37.9	56.5	86.9	88.3	99.9
Lithology		Hard grey/white mottled clay-altered (Mg-chlorite) pumiceous volcaniclastic	Mg-chlorite altered volcanic breccia	Mg-chlorite altered volcanic breccia with sulfide vein	Hydrothermal grit/gravel with aggregate clasts. Pumice replaced by Mg-chlorite.	White, hard anhydrite-clay-sulfide nodules set in Mg-chlorite altered pumiceous volcaniclastic	Pale grey hydrothermal clay (illite-montmorillonite dominated)	Pale grey hydrothermal clay (illite-montmorillonite dominated)	Light to grey coloured hydrothermal clay (Mg-chlorite dominated)	Clay-altered (Mg-chlorite) pumiceous volcaniclastic	Clay-altered (Mg-chlorite) pumiceous volcaniclastic with anhydrite vein	Clay-altered (Mg-chlorite) pumiceous volcaniclastic with anhydrite	Mottled clay-altered (Mg-chlorite) volcaniclastic
SiO_2	%	25.11	78.70	62.00	52.75	4.95	56.23	73.32	82.11	76.38	11.01	80.91	69.36
TiO_2		0.12	0.08	0.05	0.12	0.06	0.43	0.40	0.13	0.13	0.12	0.11	0.20
Al_2O_3		12.78	6.79	4.42	9.62	3.12	11.30	9.32	6.93	10.10	7.78	9.07	15.60
Fe		3.45	1.18	4.79	1.41	0.41	2.90	3.13	1.83	2.15	1.29	1.38	2.36
MnO		0.99	0.12	0.12	0.05	0.01	0.36	0.03	0.12	0.08	0.08	0.02	0.02
MgO		24.80	6.33	6.46	3.64	2.64	7.40	2.12	2.89	2.85	4.12	0.95	1.33
CaO		0.19	0.61	2.92	10.32	34.81	3.33	0.10	0.28	0.04	27.66	0.25	0.21
K_2O		0.17	0.59	0.04	1.99	0.07	1.19	2.05	1.34	2.48	1.56	2.83	4.61
Na_2O		0.51	0.21	0.03	0.57	0.25	0.92	0.62	0.24	0.45	0.30	0.36	0.41
P		0.010	0.003	0.007	0.005	0.010	0.011	0.011	0.006	0.004	0.011	0.005	0.012
Zn		15.30	0.22	3.46	0.01	0.16	0.01	0.01	0.01	0.01	0.01	0.10	0.00
Pb		0.12	0.04	0.01	0.00	0.10	0.01	0.00	0.01	0.00	0.00	0.00	0.00
Cu		0.13	0.04	1.89	0.00	0.03	0.01	0.01	0.01	0.00	0.01	0.00	0.00
BaO		<0.01	<0.01	0.02	0.04	0.03	0.06	0.02	0.06	<0.01	0.03	0.02	0.03
S		10.10	0.79	7.77	6.48	20.30	3.52	2.90	1.26	1.79	16.60	1.37	2.38
LOI		13.40	3.11	6.53	6.53	2.62	10.30	6.25	2.29	3.55	4.42	2.50	4.06
Sulfate		0.10	0.35	1.79	5.46	19.00	1.39	0.87	0.13	0.36	15.20	0.23	0.15
C		0.07	0.08	0.06	0.06	0.06	1.23	0.13	0.11	0.05	0.07	0.08	0.08
Ag	ppm	2.0	0.7	5.3	<0.1	0.4	3.0	2.6	0.1	0.1	<0.1	0.2	0.3
As		6.6	143	57.4	0.8	8.2	46.4	30.2	4.0	4.4	1.2	45.8	49.6
Ba		7.5	146	13	310	27	534	186	573	70	98	168	287
Be		1.2	3.0	1.8	2.0	0.4	2.0	2.4	1.8	2.2	0.8	1.2	2.4
Bi		3.28	2.04	9.56	0.12	0.04	0.36	0.3	0.14	0.22	0.32	0.62	5.24
Cd		318.0	7.0	101.0	0.3	4.1	0.9	0.3	0.2	0.3	<0.1	2.7	0.4
Ce		68.6	33.2	83.5	50.1	21.5	60.8	49.1	34.0	29.4	34.0	49.5	109
Cs		0.64	0.43	0.18	0.32	0.27	3.76	8.36	0.74	0.89	0.30	0.56	1.14
Dy		13.6	7.83	4.77	9.34	3.27	5.49	5.85	5.95	5.46	6.29	8.96	17.1
Er		7.92	5.76	3.43	5.82	2.05	4.3	4.49	4.06	3.98	4.38	7.01	11.7
Eu		1.46	0.45	0.62	1.25	0.67	0.85	0.66	0.79	0.6	0.69	0.55	1.51
Ga		34	13.6	13	18.8	5.1	17.9	15.8	10.9	16.7	12.9	20.0	30.3
Gd		14.5	4.97	6.49	8.94	3.63	4.8	3.92	4.69	4.26	5.54	6.35	14.8
Ge		2.95	2.65	2.45	0.35	0.35	0.95	1.4	0.55	0.45	0.35	0.55	0.60
Hf		6.91	6.6	3.68	7.68	2.41	3.77	2.74	4.16	7.52	4.91	8.45	14.00
Ho		2.88	1.95	1.17	2.12	0.76	1.37	1.39	1.41	1.32	1.46	2.18	4.11

La		34.1	15	42.4	23	11.4	31.4	26.1	17.8	13.9	15.7	22.4	50.3
Lu		1.01	0.88	0.5	0.86	0.3	0.68	0.81	0.61	0.56	0.61	1.19	1.76
Mo		6.4	4.2	8.2	9.0	5.6	8.8	1.8	2.2	4.4	2.2	6.6	9.2
Nb		12.7	11.4	6.01	13.6	3.86	12.3	11.3	8.44	8.81	8.5	13.9	23.9
Nd		37.7	17.9	43.3	29.3	11.7	29.1	21.4	17.1	14.1	19.2	26.7	57.1
Pr		9.36	4.48	10.7	7.13	2.85	7.66	5.96	4.49	3.89	4.76	6.75	15.2
Rb		6.65	21.3	1.4	37.5	2.6	51.4	98.4	45.3	74.4	42.8	96.4	140.0
Re		0.02	0.01	0.03	<0.01	<0.01	0.02	<0.01	<0.01	0.01	<0.01	<0.01	<0.01
Sb		0.9	4.1	1.6	1.1	6.4	7.1	2.9	1.7	1.3	5.6	2.1	2.2
Sc		6.3	0.6	2.7	1.2	1.1	8.5	6.5	1.9	2.7	2.5	0.2	1.9
Sm		11.9	4.17	9.6	7.67	3.19	6.02	4.31	4.22	3.37	4.93	6.62	14.5
Sn		10.4	3.4	4.0	3.6	3.0	3.2	3.0	2.0	3.2	2.2	3.4	7.4
Sr		12.6	54.2	346	561	1670	86	84.9	9.9	6.5	3840	29.6	10.4
Ta		0.85	0.77	0.44	0.89	0.27	0.85	0.65	0.55	0.81	0.55	0.93	1.7
Tb		2.39	1.08	0.94	1.52	0.6	0.86	0.77	0.86	0.85	0.98	1.24	2.61
Te		1.2	0.4	0.4	<0.2	<0.2	0.4	<0.2	<0.2	<0.2	<0.2	<0.2	0.4
Th		7.56	8.04	3.7	7.1	2.42	9.91	8.38	5.06	6.92	5.06	7.99	13.8
Tl		<0.2	0.4	0.8	<0.2	<0.2	0.8	0.6	0.2	<0.2	<0.2	0.4	0.4
Tm		0.97	1.79	0.52	0.93	0.33	0.64	0.72	0.63	0.61	0.62	1.14	1.69
U		3.7	2.94	1.2	3.25	1.95	7.12	2.73	1.67	4.17	1.19	2.66	4.12
V		8.2	4.6	9.3	1.8	2.5	67.6	63.6	6.4	1.5	1.6	2.7	15.1
W		2.75	6.25	0.85	0.80	1.80	3.60	3.45	1.05	1.80	0.25	0.7	1.15
Y		78.9	53.2	29.2	57.4	21.3	40.6	45.2	39.4	35.3	41.4	55.3	110.0
Yb		6.63	6.4	3.38	5.99	2.07	4.74	5.18	4.72	3.98	4.47	8.57	12.4
Zr		321	301	165	366	109	174	127	204	278	231	389	642
Au	ppb	7	17	14	3	6	24	14	4	4	3	31	17
Pt		<1	<1	<1	<1	<1	2	<1	<1	<1	<1	<1	1
Pd		2	2	2	2	3	8	2	2	2	2	3	3

Table 2. Scaling factors for isocon plots (Figure 7).

Site	Units	IN01 16	IN02 16	IN05 16	IN09 15	IN15 13
SiO_2	%	0.2	0.2	0.35	0.2	0.35
TiO_2		100	100	20	100	20
Al_2O_3		2.2	2.2	1.75	2.2	1.75
Fe		1.5	1.5	1.5	1.5	1.5
MnO		100	100	50	100	50
MgO		25	25	3	25	3
CaO		3	3	9	3	9
K_2O		8	8	6	8	6
Na_2O		4.75	4.75	4.75	4.75	4.75
P		2000	2000	400	2000	400
Zn		0.65	0.65	100	0.65	100
Pb		2.2	2.2	800	2.2	800
Cu		5	5	500	5	500
S		0.8	0.8	20	0.8	20
LOI		1.4	1.4	0.8	1.4	0.8
Sulfate		6	6	20	6	20
Ag	ppm	0.7	0.7	20	0.7	20
As		0.002	0.002	0.1	0.002	0.1
Ba		0.1	0.1	0.01	0.1	0.01
Bi		1	1	5	1	5
Cs		4	10	3	10	3
Eu		40	40	17	40	17
Ga		0.45	0.45	1	0.45	1
Hf		3.5	3.5	2	3.5	2
La		0.5	0.5	0.55	0.5	0.55
Mo		0.8	0.8	3	0.8	3
Nb		0.7	0.7	1.2	0.7	1.2
Rb		0.4	0.4	0.2	0.4	0.2
Sb		0.275	0.275	3	0.275	3
Sc		8	8	3.5	8	3.5
Sn		6	6	4	6	4
Sr		0.04	0.04	0.2	0.04	0.1
Ta		15	27	17	27	17
Tb		22	22	11	22	11
Te		13	13	13	13	13
Th		2	3	2	3	2
Tl		15	15	15	15	15
U		1.4	1.4	1.4	1.4	1.4
V		0.7	0.7	3	0.7	3
W		2.3	2.3	2.5	2.3	2.5
Y		0.5	0.5	0.5	0.5	0.5
Yb		3	3	2.3	3	2.3
Zr		0.3	0.3	0.05	0.3	0.05
Au	ppb	0.4	0.4	0.4	0.4	0.4

Table 3. Calculated mass change values for mobile elements in samples plotted in **Figure 8**. Mass change was calculated after the method of Grant (1986, 2004) using the immobile element isocons and equations displayed in **Figure 7**.

Site	Units	IN01 16	IN02 16	IN05 16	IN09 15	IN15 13
SiO_2	%	72.34	148.37	57.42	-5.33	25.19
Al_2O_3		-5.92	1.95	-1.80	-0.27	-3.85
Fe		200.43	19.60	37.85	0.17	-0.18
MnO		3.59	0.46	0.22	0.00	0.08
MgO		7.75	4.63	13.52	0.18	7.24
CaO		246.43	0.85	-0.34	0.07	0.20
K_2O		-0.30	0.38	-3.32	-0.18	-2.79
Na_2O		-4.30	-5.66	-5.78	-0.37	-5.79
P		875.35	128.62	0.03	0.02	0.26
Zn		356.52	0.95	0.03	0.00	0.04
Pb		77.68	3.84	0.02	0.00	0.05
Cu		849.11	87.02	39.52	-0.01	0.78
S		3.59	0.46	0.22	0.00	0.08
Sulfate		132.65	1.71	1.00	0.03	0.32
Ag	ppm	959.32	39.92	0.38	-0.01	0.74
As		763.82	55.77	71.75	3.89	170.48
Ba		1,268.72	-146.22	31.17	12.76	-106.52
Bi		361.82	123.84	37.51	-0.12	1.95
Cs		0.44	-1.70	-2.42	0.92	-2.23
Eu		0.16	0.43	-0.21	0.01	-0.17
Mo		1,023.09	21.77	23.30	-0.35	2.05
Rb		24.15	32.84	-66.12	5.12	-45.90
Sb		741.93	8.48	2.29	0.84	4.83
Sr		19,803.69	41.44	-10.45	11.89	42.74
Te		63.57	4.56	3.15	-0.01	0.28
Tl		46.18	0.75	4.58	-0.01	0.28
W		75.86	2.15	-0.59	0.18	6.56
Au	ppb	2.00	0.07	0.09	0.01	0.02

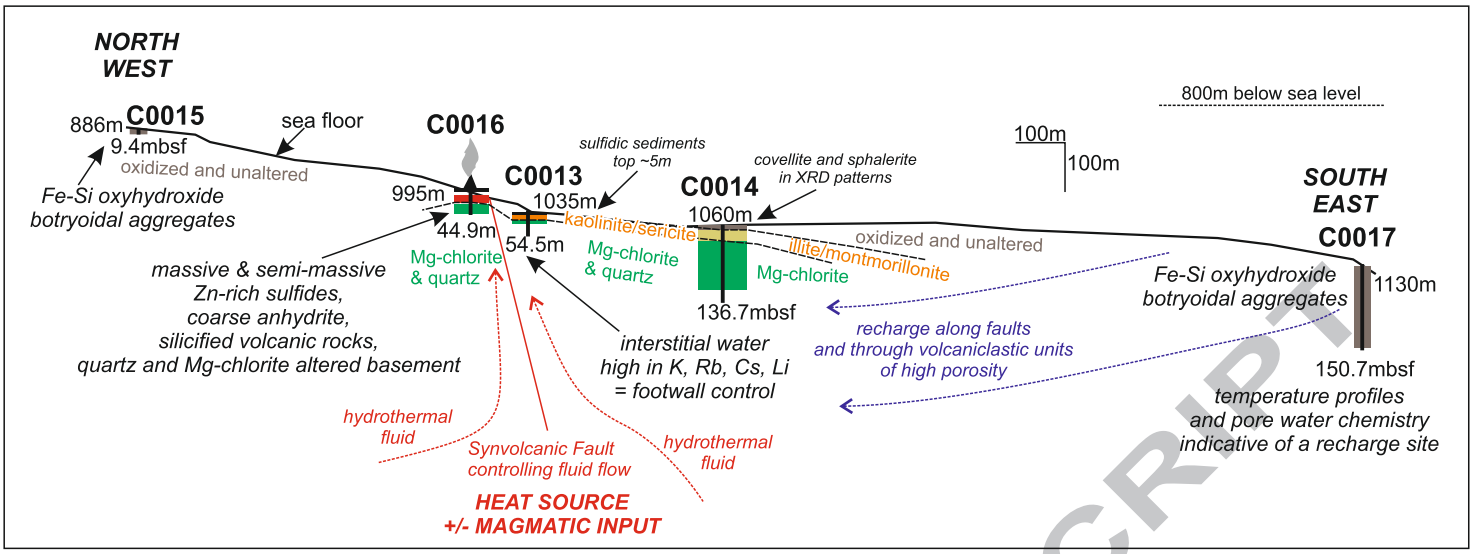

Highlights

- IODP Expedition 331 drilled five sites in the Iheya North hydrothermal field in the middle Okinawa Trough, Japan
- We present a detailed account of the system, including new whole rock geochemical, minero-chemical and microstructural constraints on recovered lithologies
- At site C0016, massive sphalerite-(pyrite-chalcopyrite±galena)-rich sulfides were intersected
- Underlying volcanic rocks exhibit quartz-muscovite/illite and quartz-Mg-chlorite alteration
- The Iheya North hydrothermal system represents a modern analogue for Kuroko-type VHMS mineralization